Engineered Science
DOI: https://dx.doi.org/10.30919/es1735

Oxygen Vacancy Modulation via Confinement: Enhanced Dry Reforming Activity and Stability of Nickel-Cerium Catalysts Encapsulated in Titanium Silicalite-1 Zeolite

Huabing Zhang,[1, 3] Dandan Sun,[1] Xinyue Zhang,[1] Jin He,[1] Houxiang Sun,[1, 3,*] Haiyan Yang,[1, 3] Zhiqiang Jiang,[2, 3,*] Yani Liu,[1] Furong Li[1] and Wenwu Zhou[4,*]

Abstract

The advancement of anti-coking catalysts for dry reforming of methane (DRM) is essential for mitigating greenhouse gas emissions and promoting sustainable syngas production. Herein, a series of nickel-cerium (CeNi@TS-1) catalysts for the DRM was synthesized via impregnation-recrystallization. Among these, 12CeNi@TS-1 exhibited markedly superior catalytic activity achieving conversion rates of 81.2% for methane (CH_4) and 92.3% for carbon dioxide (CO_2), with specific activities of 4.83 $mmol_{CH4}·g_{Ni}^{-1}·s^{-1}$ and 5.48 $mmol_{CO2}·g_{Ni}^{-1}·s^{-1}$. For 12CeNi@TS-1 following 50 h of operation, minimal activity loss of less than 0.5% was observed for both CH_4 and CO_2, indicating good stability. Physical and morphological analyses revealed that appropriate CeO_2 content effectively reduced and dispersed the nickel (Ni) nanoparticles (NPs) while maintaining the MFI structure, also enhancing the interactions between the Ni NPs, TS-1, and ceria (CeO_2). This modification fostered a rich environment of oxygen vacancies (OVs). Hence, the prevalence of Ni NPs in stronger electron-deficient states was increased, along with the number of basic sites conducive to synergistic activation of CH_4 and CO_2. In-Situ DRIFTS spectroscopy analysis indicated that CeO_2 introduction in 12CeNi@TS-1 enhanced the CH_4 and CO_2 activation, while suppressing excessive CH_4 cracking and carbon accumulation by OVs. This work provides significant insights into the effective utilization of greenhouse gases for sustainable energy conversion.

Keywords: Methane dry reforming; metal Ni NPs; oxygen vacancies; TS-1 zeolite; CeO_2.
Received: 16 July 2025; Revised: 26 August 2025; Accepted: 21 September 2025.
Article type: Research article.

1. Introduction

The substantial emission of greenhouse gases, particularly carbon dioxide (CO_2), plays a crucial role in the increase of global temperatures and heightened frequent extreme weather events. To alleviate these challenges and enhance human well-being, numerous countries around the globe have implemented a variety of strategies focused on energy conservation and emission reduction. Concurrently, as global energy demand to rise, coupled with the challenges presented by climate change and the growing need for alternative energy sources, dry reforming of methane (DRM) has gained significant attention and significance in recent years. DRM is an endothermic reaction that produces syngas-a mixture of hydrogen (H_2) and carbon monoxide (CO)-through the utilization of CO_2 and CH_4, both of which are greenhouse gases.[1,2] Syngas can be effectively utilized and converted into a variety of valuable chemicals. DRM is recognized as a more efficient and environmentally sustainable method for high-value energy conversion. However, DRM is an endothermic process that requires high temperatures to achieve significant conversion rates of both CO_2 and CH_4.[3,4] Consequently, the energy consumption associated with syngas production constitutes over 50% of the total chemical reaction chain. Therefore, it is imperative to introduce innovative low-energy technologies into DRM to facilitate the "green" development

[1] *School of Biology and Chemical Engineering, Sichuan Technology & Engineering Research Center for Vanadium Titanium Materials, Panzhihua University, Panzhihua, 617000, China*
[2] *School of Vanadium and Titanium, Panzhihua University, Panzhihua, 617000, China*
[3] *Vanadium and Titanium Critical Strategic Materials Key Laboratory of Sichuan Province, Panzhihua University, Panzhihua, 617000, China*
[4] *College of Chemistry and Chemical Engineering, Xi'an University of Science and Technology, Xi'an 710054, China*
[*] *Email*: sunhouxiang8402@163.com (H. Sun); jiangzq@pzhu.edu.cn (Z. Jiang); Zhww1015@163.com (W. Zhou)

of chemical synthesis pathways. The advancement of novel catalytic systems represents a critical step toward enhancing reactant conversion efficiencies, improving reaction stability, and reducing overall reaction energy consumption.

The DRM reaction requires the presence of a catalyst, which is typically composed of a noble or transition metal supported on an appropriate substrate. Nickel (Ni) demonstrates a reactivity level comparable to that of noble metals while being more cost-effective, thus providing significant advantages for large-scale applications.[4,5] However, two predominant challenges persist: activity reduction due to carbon deposition and inadequate resistance to thermal sintering.[6,7] The thermal sintering resistance of these catalysts can be enhanced by improving the interaction between the metal and support; however, significant challenges related to carbon deposition persist.[8] Specifically, carbon deposition partially diminishes the catalyst activity and may even lead to complete deactivation. It is widely acknowledged that carbon deposition arises from side reactions occurring during the DRM process, such as $CO+H_2 \rightarrow C+H_2O$, $CH_4 \rightarrow C+2H_2$, and $2CO \rightarrow C+CO_2$. These reactions impede the timely conversion of deposited carbon, resulting in its gradual accumulation.[9,10] This accumulation subsequently obstructs channels and reduces the number of exposed active sites, ultimately leading to the catalyst. Therefore, it is imperative to design and develop highly efficient Ni-based DRM catalysts with superior anti-coking and sintering properties to enhance applicability in practical industrial environments. During the design and development process, various parameters may necessitate adjustment, including the acidity and alkalinity levels, considerations of electronic structure, the formation of oxygen vacancy (OV), particle size distribution, exposure of active sites, dispersion of active metal, incorporation of secondary metal, generation of reactive oxygen species, as well as the selection of appropriate promoters and supports.[11,12] Among these variables, the formation of OVs and the incorporation of suitable promoters are particularly critical to the DRM reaction.

Catalyst construction involves more than simply selecting active metals; it requires a careful selection of support materials. The type of support plays a critical role in determining the key properties (*i.e.*, activity, stability, and selectivity) of Ni-based DRM catalysts.[13] Typically, supports having rich pore structure are employed, as this significantly enhances the reactive mass transfer and promotes the dispersion of active metals. Consequently, zeolites with abundant porosity are ideal candidates.[14] Due to their exceptional properties, including tunable heteroatom compositions, high specific surface areas, and well-defined nanoscale pores, these materials are widely employed as support materials, heterogeneous catalysts, and adsorbents.[15-17] Among the various zeolites, the TS-1 zeolite is notable for its alkaline surface and MFI topology, with some Si atoms in the framework being replaced by Ti atoms.[18] Notably, the TS-1 zeolite has demonstrated commendable performance in catalytic applications.[19,20] The primary factors influencing this catalytic activity include the coordination environment, electronic structure, and acid-base properties of the Ti centers within the Si matrix.[21] This can be ascribed to the interaction between the supported active metals and the Ti atoms of TS-1 zeolite, which modulates both the electronic structure of these metals and their dispersion. In previous work by Liu *et al*. a catalyst was developed that employed Pt to generate sub-nanometer metal species (single atoms and clusters) on TS-1 zeolite.[22] The support featured an abundant silicon (Si) and titanium (Ti) hydroxyl groups, as well as Lewis basic sites, while exhibiting a high specific surface area. These attributes facilitated robust interactions with the active metals, effectively preventing thermal sintering of active phase structures. Moreover, this support significantly improved the reactant transport while mitigating coking reactions. Throughout the reaction process, exceptional levels of catalyst activity, stability, and selectivity were observed.

Typically, to enhance the efficacy and stability of DRM catalysts, a secondary component is introduced as a promoter. Over the past decade, this strategic approach has garnered significant interest,[23] accompanied by extensive research on traditional oxide materials (including Al_2O_3, MgO, TiO_2, ZrO_2, and SiO_2.[26-28]) However, the activity and durability of these Ni catalysts remain unsatisfactory. Specifically, the catalysts derived from neutral SiO_2 and acidic Al_2O_3 operate under a single-functional mechanism for the activation of CO_2 and CH_4, yielding suboptimal catalytic efficiency.[29,30] Furthermore, the acidic surfaces of these materials effectively facilitate cleavage of the CH_4 molecule, leading to the production of significant amounts of carbon species.[31] Concurrently, their low reactivity diminishes the interactions between the metal and support,[32] which adversely impacts sintering resistance. This distinction arises from the fact that catalysts synthesized using the alkaline surfaces of TiO_2 and MgO activate CO_2 and CH_4 via a bifunctional mechanism.[29,30] Their oxygen mobility and redox properties are relatively constrained, resulting in less pronounced formation of medium-strength basic sites.[32,33] Consequently, this limitation reduces the effectiveness of carbon species gasification and leads to suboptimal performance in mitigating metal sintering and carbon deposition.[34]

When CeO_2 is employed as a promoter, there is a significantly enhanced in catalytic activity, stability, and carbon species removal.[35,36] This improvement can be attributed to the remarkable redox properties and abundant surface defects of CeO_2. Indeed, due to the distinctive redox cycling between Ce^{3+} and Ce^{4+}, CeO_2 exhibits remarkable oxygen mobility and is regarded as an exemplary material.[37] Form a defect chemistry perspective, the loss of oxygen within the lattice is considered a source of OV.[38] Moreover, the incorporation of lower-valence Ni^{2+} into the host structure of CeO_2 can induce lattice distortion that generates additional Ovs.[39] The surface OVs on CeO_2 act as optimal sites for CO_2

activation, thereby facilitating the DRM process. Furthermore, the dissociation of CO_2 molecules results in the formation of CO* and O*, which can occupy the available OVs present on the CeO_2 surface. This process enhances the catalyst longevity by promoting gasification of the deposited carbon during DRM reaction.[40] When employed as a promoter for Ni-based catalysts, CeO_2 not only modulates the electronic structure and dispersion of metallic Ni but also fine-tunes the Lewis acid-base sites. This behavior significantly enhances the activity and stability while simultaneously mitigating the carbon species formation.[41] Amin *et al*.[42] demonstrated that, compared to other catalysts, a Ni-based catalyst doped with CeO_2 exhibited considerably higher conversion rates of CH_4 and CO_2 (83% and 99%), along with the minimal carbon deposition beyond 60 h. This remarkable performance can be ascribed to the optimal interactions between the metallic Ni, zeolite, and CeO_2, which create favorable acid-base sites and an exceptional electronic structure within the catalyst. Consequently, it is now widely recognized that CeO_2-doped DRM catalysts possess significant industrial applications potential.[43]

Herein, Ce^{3+}-Ni^{2+}/TS-1 was employed as a substitute for CeO_2-NiO/TS-1 to serve as the precursor for synthesizing CeNi@TS-1 catalyst. This synthesis was conducted in a tetrapropyl ammonium hydroxide solution via the "dissolution-recrystallization" method. During the recrystallization process, modifications were made to the TS-1 lattice through the incorporation of Ce and Ni dopant atoms, resulting in the formation of new chemical bonds. Consequently, CeO_2 and NiO nanoparticles (NPs) became integrated with the TS-1 zeolite; these NPs were embedded within the TS-1 shell rather than residing in its pores during calcination. This distinctive synthesis strategy facilitated a high degree of dispersion (<5 nm) for the Ni NPs, even when the total loading of CeO_2 and Ni is 20 wt%, which poses a significant challenge for the metal catalysts synthesis. Furthermore, incorporation of CeO_2 led to the formation of abundant OVs within the DRM catalysts, effectively mitigating carbon deposition. The TS-1 zeolite, which was embedded with uniformly distributed CeO_2 and Ni NPs, exhibited a dual physical and chemical constraint structure along with abundant OVs. In particular, the 12CeNi@TS-1 catalyst (having 12 wt% CeO_2 input content) demonstrated excellent catalytic performance and stability over a duration of 50 h. This unique configuration enabled the CeNi@TS-1 catalyst to achieve excellent activity and stability of DRM.

2. Experiment

2.1 Catalyst synthesis

Tetrapropylammonium hydroxide (25%, TPAOH), isopropyl alcohol (99% $CH_3CHOHCH_3$), tetrabutyl titanate (99% TBOT), tetraethyl orthosilicate (TEOS), cerous nitrate (98%, $Ce(NO_3)_3{\cdot}6H_2O$), nickel nitrate (98%, $Ni(NO_3)_2{\cdot}6H_2O$), were purchased from Macklin Company. Ethanol was sourced from Sinopharm Chemical Reagent Co., Ltd. All the chemicals were utilized without any prior purification.

Preparation of TS-1 zeolite: First, 46.72 g of TPAOH (25 wt%), 11.68 g of deionized water, and 40.00 g TEOS were completely mixed with 2.64 g TBOT in an ice bath for 60 min. The mixture was then heated to 70 °C and stirred continuously for 180 min. Next, 48.00 g of isopropyl alcohol was added and the mixture was stirred for 60 min. Finally, the prepared solution was transferred to a teflon autoclave and allowed to crystallize statically at 170 °C for 4 d. After cooling, the solid product was centrifuged and dried at 120 °C for 12 h. Finally, TS-1 zeolite was synthesized through calcination in static air at 550 °C for 6 h.

Preparation of CeNi@TS-1 catalysts (Fig. 1a): The preparative TS-1 zeolite was treated with a mixed aqueous solution of $Ni(NO_3)_2{\cdot}6H_2O$ and $Ce(NO_3)_3{\cdot}6H_2O$ (1.0 g zeolite: 2.5 mL solution and Ni: CeO_2: TS-1= 5 wt%: *x* wt%: 100-5-*x* wt%, *x*=0, 3, 6, 9,12 and 15). The mixture was subsequently mixed at room temperature until the water had evaporated completely. Ni-Ce-impregnated crystals in a 0.3 M TPAOH solution (1.0 g zeolite: 35 mL solution) were treated at 170 °C for 3 d, such that the Ni and Ce were encapsulated within the TS-1 crystals. The prepared samples were collected via centrifugation and dried at 120 °C for 12 h. The organic templates were removed through calcination at 540 °C for 4 h. The resulting catalysts were labeled as *x*CeNi@TS-1 (Ni@TS-1, 3CeNi@TS-1, 6CeNi@TS-1, 9CeNi@TS-1, 12CeNi@TS-1, and 15CeNi@TS-1, respectively).

2.2 Characterization

The characterisation of samples via X-ray diffraction (XRD) was conducted using a PANalytical X'Pert powder diffractometer equipped with Cu Kα radiation in the range of 10 to 80° at $10°{\cdot}min^{-1}$. The surface environments of the samples were measured using X-ray photoelectron spectroscopy (XPS, ThermoFisher, K-Alpha, America) spectroscopy with a Thermo Fisher K-Alpha spectrometer at 1486.6 eV with a sensitivity of 1.0 eV (650 μm). UV-Visible spectra (UV-Vis) were measured in the wavelength 200-600 nm wavelength range using a spectrophotometer (CERNET, PE Lambda950, China). Raman analysis was conducted using a Raman spectrophotometer equipped with 325 nm He-Ne laser (Raman, Renishaw, InVia Qontor, England), recording data from 200 to 1500 cm^{-1}. Fourier transformed infrared (FTIR) analysis was conducted using a ThermoFisher Nicolet iS10 in the wavenumber range of 600 to 2000 cm^{-1}. The specific surface area and pore structure data of the catalysts were tested using a nitrogen adsorption system (Micrometritics, TriStar 3020) at the liquid-nitrogen temperature of 77 K with the Brunauer-Emmett-Teller (BET) method. The concentrations of elements in the samples were determined using inductively coupled plasma spectrometry (ICP, Perkin Elmer, Nex ION 350D, England). The specific surface area and pore structure of the samples were determined through nitrogen physisorption measurements using a Micromeritics TriStar 3020 equipment. Scanning electron

microscope (SEM, Carl Zeiss AG, Ultra Plus, Germany) and high-resolution transmission electron microscopy (HRTEM, ThermoFisher, FEI F2100) were used to perform the morphological observations of the samples. Energy Dispersive Spectroscopy (EDS) was used to obtained the elements distribution of the catalysts. The determination of programmed temperature desorption of carbon dioxide (CO_2-TPD) and temperature-programmed reduction of H_2 (H_2-TPR) was conducted using a Micromeritics Autochem 2920 instrument with a thermal conductivity detector (TCD) and a computer-controlled CryoCooler. The reduction profiles of H_2-TPR were measured by passing a 50 mL·min^{-1} 10% H_2/Ar through the sample. The temperature was raised from 100 to 850 °C at 10 °C·min^{-1}, while the H_2 consumption was monitored using TCD. The catalysts were subjected to a 50 mL·min^{-1} CO_2 flow for 90 min. After stabilizing the baseline of the CO_2 signal, the CO_2-TPD was performed with a ramping rate of 10 °C·min^{-1} up to 800 °C under an Ar stream. A thermogravimetric analyzer was employed to conduct the thermogravimetry (TG, Netzsch, STA449F5, Germany) of the spent samples with the temperature rising from 25 to 800 °C at a rate of 10 °C·min^{-1}.

In situ DRIFTS measurements (In-Situ DRIFTS) was used the same FTIR instrument (ThermoFisher, Nicolet iS50, China) equipped with a liquid-nitrogen-cooled MCT detector. A high temperature reaction cell (Harrick) was connected to a gas-dosing device featuring mass flow controllers. The catalysts were placed into a ceramic crucible within the cell. The temperature was then lowered to 50 °C under N_2 atmosphere. The background spectra were obtained at 50 °C in N_2 environment. Then, the system was switched to a mixed gas flow of CH_4/CO_2/N_2 (1/1/2), while gradually increasing the temperature. Subsequently, the alterations of the DRIFTS spectra were recorded at 60 s intervals with a resolution of 1 cm^{-1}. This procedure was accomplished by incrementally raising the temperature of the catalyst from 50 to 500 °C at a rate of 10 °C·min^{-1}. Afterward, N_2 was used for purging at 500 °C for 30 min, and the background spectra were obtained at the same temperature under N_2. Under isothermal conditions, the gas mixture CH_4/CO_2/N_2 (1/1/2) was introduced into the cell, and the DRIFTS spectra were conducted every 60 s for 30 min.

2.3 Catalytic activity test

The DRM performance of each synthesized samples was investigated in a continuous-flow fixed-bed reactor. A mixture of 40-60 mesh particles, comprising the catalyst (0.1000 g) and quartz sand (1.0000 g), was introduced to a quartz tubular reactor. Before testing, the fresh catalyst was heated at 750 °C in an N_2 atmosphere (40 mL/min). Subsequently, the catalyst was reduced for 60 min using a mixture of H_2 and N_2 (20 and 40 mL/min, respectively). The mixture was then cooled or heated in an N_2 atmosphere to the specified temperature before switching to the reactants (CH_4/CO_2/N_2 = 4/4/2) at a gas hourly space velocity (GHSV) of 60 L/g^{-1}·h^{-1}. The produced gas was performed utilizing an online gas chromatograph (Huifen 901A, China). The conversions, reaction rates, and H_2/CO ratio were determined using the following Eqs. (1)-(5):

$$CH_4 \text{ conversion} = X_{CH_4} = \frac{F_{CH_4,in} - F_{CH_4,out}}{F_{CH_4,in}} \times 100\% \quad (1)$$

$$CO_2 \text{ conversion} = X_{CO_2} = \frac{F_{CO_2,in} - F_{CO_2,out}}{F_{CO_2,in}} \times 100\% \quad (2)$$

$$CH_4 \text{ reation rate} = k_{CH_4} = \frac{F_{CH_4,in} - F_{CH_4,out}}{m_{cat} \times V_m} \quad (3)$$

$$CO_2 \text{ reation rate} = k_{CO_2} = \frac{F_{CO_2,in} - F_{CO_2,out}}{m_{cat} \times V_m} \quad (4)$$

$$H_2/\text{CO} = \text{R}_{H_2/CO} = \frac{F_{H_2,out}}{\text{F}_{\text{CO, out}}} \quad (5)$$

Here, $F_{CO2,in}$, $F_{CO2,out}$ $F_{CH4,in}$, and $F_{CH4,out}$, are the CO_2 and CH_4 flow rates in the feed or outlet, repectively; V denotes the CH_4 or CO_2 flow rate; X denotes the CH_4 or CO_2 conversion rate; m_{cat} indicates the mass of the corresponding catalyst; and V_m is the standard molar volume.

3. Results and discussion

3.1 Structural analysis

3.1.1 XRD characterization

The XRD patterns of the six oxide CeNi@TS-1 catalysts within 5-80º are presented in Figs. 1b-c. Only peaks associated with the MFI topology were detected,[20] and no peaks corresponding to CeO_2 (JCPDS No. 75-0390) or NiO species (JCPDS No. 71-1179) were observed.[36] In compared to Ni@TS-1, the introduction of increasing amounts of CeO_2 discernibly reduced the characteristic peaks associated with the MFI topology. This observation indicates that the incorporation of CeO_2 facilitated a more uniform dispersion of Ni, which resulted in a decrease in the Ni NP size. As displayed in Fig. 1b, with the addetion of Ce and Ni species, the TS-1 peaks shifted notably towards lower angles, this can be ascribed to the substitution of Ce or Ni for Si during the recrystallization process, leading to an enlargement of the unit cell volume of the zeolite.[44]

3.1.2 UV-vis and FTIR analysis

The UV–Vis spectra of the six prepared catalysts are shown in Fig. 1d. It is well established that, in contrast to bulk Ni, Ni NPs exhibits distinct photoelectric properties. When incident light interacts with the surfaces of Ni NPs, it excites the free electrons, leading to the surface plasmon resonance (SPR) phenomenon. This effect generates characteristic resonances at approximately 280 nm in the UV-Vis region.[45] However, none of the six CeNi@TS-1 catalysts displayed the characteristic peaks associated with Ni NPs. Instead, signal peaks corresponding to -Ni-O-Si- species were observed at 218 nm.[46] This outcome indicates that the Ni NPs were uniformly dispersed with a small particle size, which is consistent with the XRD results. Furthermore, within the UV-Vis spectral range of 250-320 nm, all six catalysts exhibited

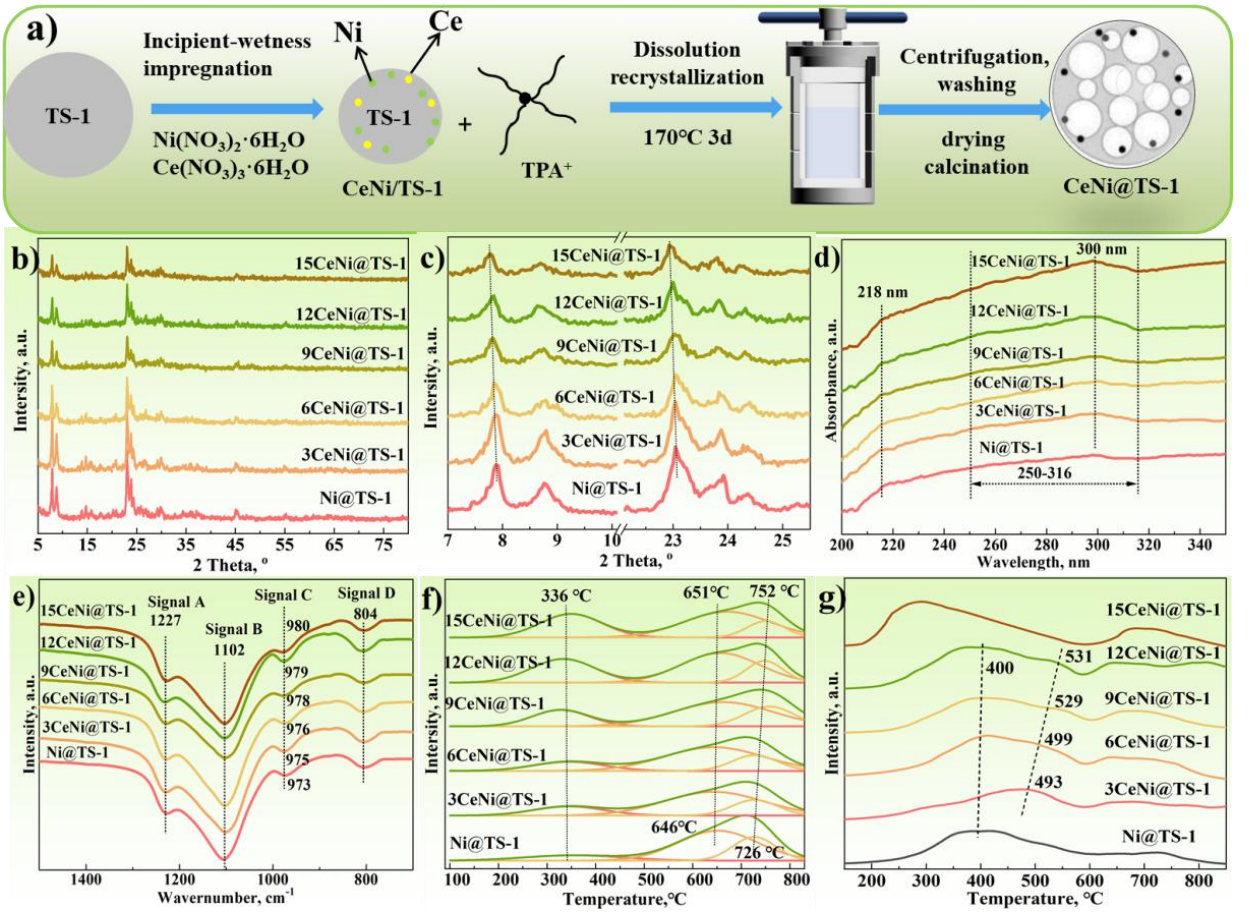

Fig. 1: Schematic diagram of CeNi@TS-1 catalysts synthesis (a), XRD patterns (b, c), Raman (d), UV-Vis (e), FT-IR (d), H_2-TPR (f), and CO_2-TPD (g) results of six oxide catalysts.

prominent broad-band responses; this phenomenon can be ascribed to the octahedral coordination of Ni^{2+} within the NiO cluster, facilitating the charge transfer transition from O^{2-} (2p) to Ni^{2+} (3d).[47] Additionally, the introduction and subsequent increase in CeO_2 content resulted in a signal peak at 300 nm compared to that observed Ni@TS-1.[44] However, this peak remains predominantly characterized by a broad feature associated with -Ce-O-Si- species.[48]

The FTIR spectra of the six samples are displayed in Fig. 1e. The peaks observed at approximately 1227, 1102, 973, and 804 cm^{-1} (signal A-D, respectively) correspond to the stretching vibrations of the framework, asymmetric stretching vibrations of the [SiO_4] units, stretching vibrations associated with Ti-O-Si bonds, and symmetric vibrations of the [SiO_4] units, respectively.[18] As the content of CeO_2 increased, the positions and intensities of signals A, C, and D remained largely consistent. This behavior suggests that the [SiO_4] units and framework exhibit remarkable stability against disruption. In contrast, the signal B intensity gradually decreased while a blueshift phenomenon was observed. This observation can be interpreted as indicating of partial disruption of the Ti-O bonds within the Ti-O-Si material,[18,49] which is consistent with the decrease in peak intensity noted in the XRD results.

3.1.3 Textural properties and ICP analysis

The specific surface areas and pore structures of the six catalysts were determined using the Brunauer-Emmett-Teller (BET) method, as presented in Table 1. Fig. S1 displays the results of N_2 adsorption–desorption isotherms. The adsorption characteristics of the six observed catalysts were notably pronounced at low relative pressures (P/P_0 <0.01) and distinct hysteresis loops were observed within 0.2–0.8 P/P_0, indicating the presence of microporous and mesoporous structures.[50] All the examined catalysts exhibited Type IV isotherms, accompanied by comparable specific surface areas and pore volumes. As the concentration of Ce increased, there was a significant reduction in both the specific surface area and pore volume. This alteration can be attributed to the rising number of Si atoms within the substituted framework. This alteration disrupted certain portions of the MFI framework in the zeolite, leading to a reduction in the specific surface area and pore volume,[51] as shown in Table 1. This outcome is consistent with the XRD results. The actual contents of CeO_2 and Ni in six catalysts were determined through ICP analysis, with results presented in Table 1. All six samples exhibited comparable Ni content, approximately 5 wt%. However, the CeO_2 concentration increased in accordance with the amount added. The mass percentages of CeO_2 and Ni in the samples

Table 1: Chemical composition, textural and pore structure data for six samples.

Samples	S_{BET} $m^2 \cdot g^{-1}$	S_{micro} $m^2 \cdot g^{-1}$	S_{meso} $m^2 \cdot g^{-1}$	V_{pore} $cm^3 \cdot g^{-1}$	V_{micro} $cm^3 \cdot g^{-1}$	V_{meso} $cm^3 \cdot g^{-1}$	Ni content[a] wt%	CeO_2 content[a] wt%
Ni@TS-1	438	204	234	0.732	0.106	0.626	5.2	0.0
3CeNi@TS-1	417	174	243	0.687	0.090	0.597	5.5	2.6
6CeNi@TS-1	397	186	211	0.674	0.096	0.578	5.4	6.1
9CeNi@TS-1	398	161	237	0.666	0.083	0.583	5.3	9.6
12CeNi@TS-1	388	146	242	0.624	0.079	0.545	5.0	14.7
15CeNi@TS-1	374	142	232	0.606	0.077	0.529	4.9	16.6

a Determined via ICP analysis

closely align with the theoretical values. The BET data (Table 1 and Fig. S1) provide a more detailed insight into the structure integrity of the channel across the six samples, thereby indirectly confirmed the embedded Ce and Ni NPs configuration.

3.2 Chemical structure analysis

3.2.1 H_2-TPR analysis

The reduction performances of all oxide catalysts were obtained using H_2-TPR. As illustrated in Fig. 1f, a reduction peak was observed at approximately 336 °C for NiO, which can be attributed to the weak interaction between the metal and its support.[52] In contrast, the Ni species that were strongly bound and embedded within the layered silicate lattice structure underwent reduction at 500-800 °C. It is noteworthy that the reduction peak identified in Ni-phyllosilicate species is associated with the octahedral Ni^{2+} sites.[52] Generally, the peak centered around 650 °C indicates 1:1 phyllosilicates,[52,53] whereas the peak located at 750 °C (a reduction temperature that exceeds 710 °C) is attributed to 2:1 phyllosilicates.[52,53] In this study, as the CeO_2 content increased, the NiO species reduction peaks progressively intensified, and the high-temperature reduction peak associated with layered silicates shifted from 726 to 752 °C. Notably, when the CeO_2 content was maximized, for 15CeNi@TS-1, the center of this reduction peak exceeded 750 °C. This property may be ascribed to the enhanced Ni NP dispersion facilitated by the increased CeO_2 volume, which facilitated a greater number of reducible species. Additionally, the interaction between the support material and embedded Ni NPs gradually strengthened.

3.2.2 CO_2-TPD analysis

The CO_2-TPD was employed to determine the surface basicity of each sample. Note that the desorption peaks corresponding to weak CO_2 can be classified into three distinct categories: strong (>550 °C), medium strength (250-550 °C), and weak (<250 °C) basic sites, which are attributed to surface coordinated unsaturated O^{2-}, metal–oxygen pairs and surface –OH groups.[54] Both strong and weak basic sites are deemed inactive within the high-temperature range of DRM. Thus, only medium-strength basic sites play a significant role in facilitating CO_2 adsorption and regulate excessive CH_4 cracking.[55,56] As illustrated in Fig. 1g, diverse distributions of medium-strength basic sites are evident for all catalysts within 250-550 °C. For all samples except for 15CeNi@TS-1, a signal peak was observed at approximately 400 °C; this peak corresponds to the formation of medium-strength basic sites resulting from strong metal-oxygen pairs between the Ni NPs and TS-1.[57] Notably, with the introduction and increased concentration of CeO_2, an additional signal peak emerged at approximately 500 °C and gradually shifted towards higher temperatures. This behavior can be ascribed to a reduction in the Ni NP size due to enhanced presence of CeO_2, which likely caused stronger interactions. This observation aligns with the results obtained from the H_2-TPR analysis. However, for the 15CeNi@TS-1 catalyst at 500 °C, there was a sudden decrease in intensity of the moderate-strength basic sites. This behavior can be ascribed to substantial coverage of the Ni nanoparticles by the CeO_2, which inhibited the formation of fully exposed Ni-O-*X* species. Consequently, only an optimal CeO_2 quantity can ensure adequate exposure at moderate intensity positions, while facilitating CO_2 activation and suppressing CH_4 cracking. This outcome is advantageous for the DRM reaction.

3.2.3 XPS analysis

To conduct a comprehensively investigation the electronic effects, XPS was employed for high-resolution analyses of the Ni, Ce, O, Si, and Ti of the six catalysts. The results of XPS are presented in Fig. 2, and Fig. S2. The O 1s fitting spectrum at approximately 530.45 and 532.75 eV (Fig. 2a) revealed two chemical states of O on the surfaces of the six catalysts, corresponding to the lattice and chemisorbed oxygen (O_{lat} and O_{ads}), respectively.[58,59] The OVs can capture adsorbed oxygen.[59,60] Consequently, an increased proportion of adsorbed oxygen generally leads to a higher OV concentration within the catalysts. The variation in the $O_{ads}/(O_{lat}+O_{ads})$ ratio revealed a trend that initially increases and subsequently decreasing. The maximum adsorbed oxygen content was measured at 7.7% for the 12CeNi@TS-1 catalyst, indicating a greater number of OVs (Table 2) compared to in the other catalysts. It is widely acknowledged that OVs play a significant role in facilitating carbon elimination process, thereby enhancing the durability of DRM catalysts.[43,47] With the incorporation of Ce into the framework, the O1s peaks of the CeNi@TS-1 catalysts shifted towards higher binding energies; this observation further substantiates the conclusion that the Ce was integrated into the framework of the TS-1 zeolite, as indicating by previous structural characterization

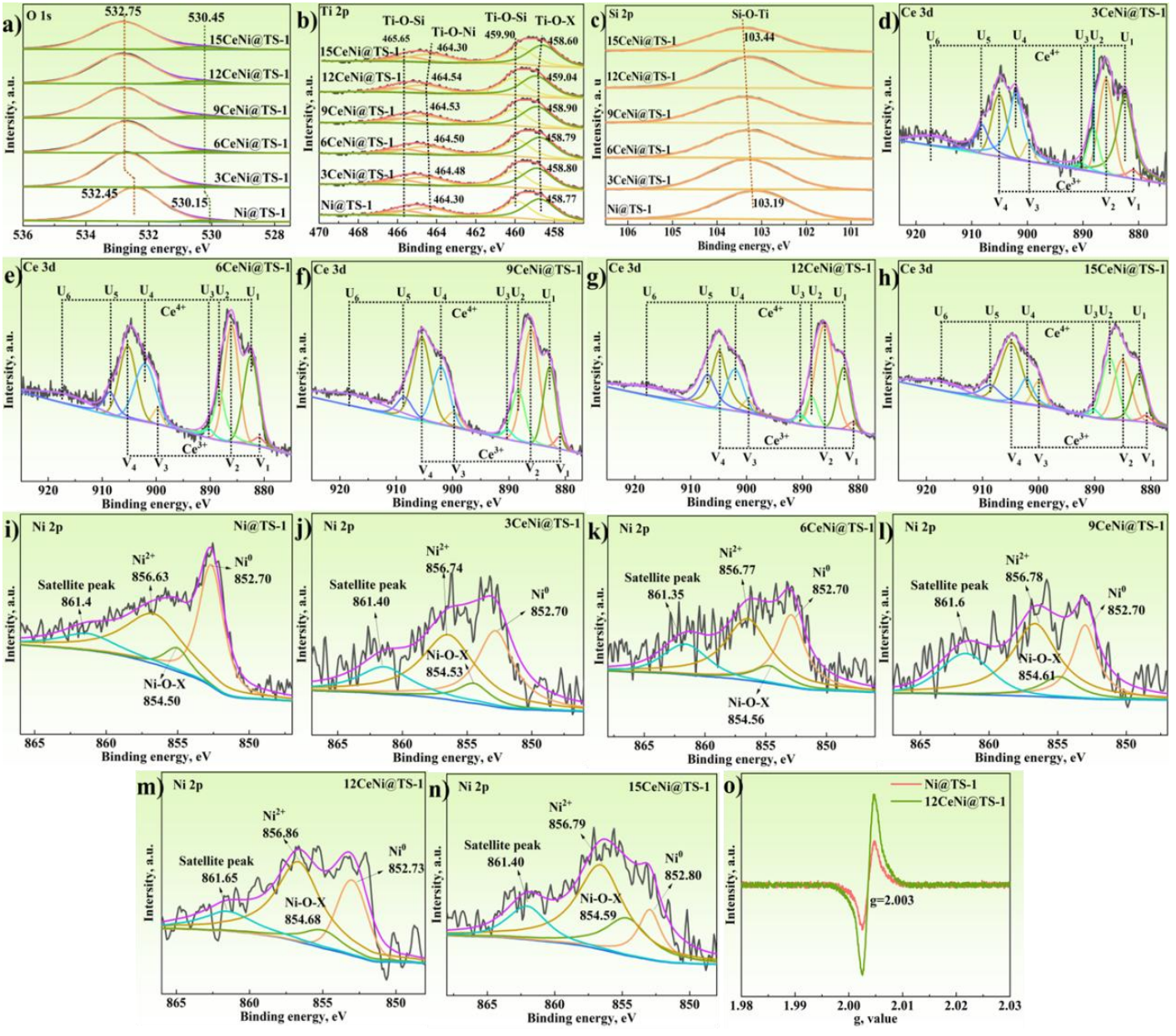

Fig. 2: XPS and EPR analysis of various reduced catalysts: (a) O 1s, (b) Ti 2p, (c) Si 2p, (d-h) Ce 3d, (i-n) Ni 2p, and (o) EPR.

findings.

Fig. 2b displays the Ti 2p spectra of the six catalysts. In pure TS-1, two signals corresponding to Ti-O-Si were observed at approximately 459.9 and 465.7 eV.[61,62] Notably, upon incorporating Ce and Ni NPs into the TS-1, a new set of peaks emerged. These peaks are likely associated with Ti-O-Ni (458.80 and 464.50 eV), resulting from the interaction between the TS-1 and Ni NPs that facilitated electron transfer from the Ni NPs to the Ti atoms.[21] Compared with Ni@TS-1, increasing CeO_2 contents (from 3CeNi@TS-1 to 12CeNi@TS-1) resulted in a positive shift in the Ti-O-Ni signal. This observation indicates a stronger interaction between the Ce or Ni and TS-1, which was characterized by enhanced electron transfer from the Ni NPs to the Ti atoms.[56,63] Interestingly, in contrast to the result for 12CeNi@TS-1, for 15CeNi@TS-1, adding CeO_2 led to a gradual negative shift of the Ti-O-Ni peak. This indicates a weakening of the interaction between the TS-1 and Ni NPs, which was accompanied by reduced in electron transmission efficiency. The interaction ratio between the Ti atoms and Ni NPs was assessed based on the molar ratio of Ti-O-Ni to Ti-O-Si, referred to as Ti-O-Ni/Ti-O-Si value; the relevant data are presented in Table 2. This ratio can also be interpreted as indicating Ni NPs with the TS-1 or the quantity of Ti-O-Ni species. The maximum Ti-O-Ni/Ti-O-Si value was obtained for 12CeNi@TS-1. A decreasing trend was observed following this order: 12CeNi@TS-1 (1.714) >15CeNi@TS-1 (1.631) > 9CeNi@TS-1 (1.569) >6CeNi@TS-1(1.467)> 3CeNi@TS-1(1.416)> Ni@TS-1(1.405). In comparison with Ni@TS-1, incorporating CeO_2 significantly reduced the Ni NP volume, yielding in smaller particle sizes within 12CeNi@TS-1. In catalysts exhibiting similar Ni content, smaller Ni NP size

Table 2: The XPS data for various reduced catalysts.

Samples	Ni@TS-1	3CeNi@TS-1	6CeNi@TS-1	9CeNi@TS-1	12CeNi@TS-1	15CeNi@TS-1
$O_{ads}/O_{ads}+O_{lat}$, %	1.8	3.2	4.1	5.4	7.7	6.3
$I_{Ni0}/I_{Ni0}+I_{Ni2+}+I_{Ni-O-X}+I_{NiSate}$, %	37.6	33.6	30.6	23.9	22.9	14.7
$I_{Ni2+}/I_{Ni0}+I_{Ni2+}+I_{Ni-O-X}+I_{NiSate}$, %	41.3	41.7	43.0	44.6	51.4	50.3
$I_{Ni-O-X}/I_{Ni0}+I_{Ni2+}+I_{Ni-O-X}+I_{NiSate}$, %	7.2	7.8	8.8	9.9	10.7	20.7
$Ce^{3+}/Ce^{3+}+Ce^{4+}$, %	---	35.2	42.4	48.0	51.1	47.4
Ti-O-Ni/Ti-O-Si	1.405	1.416	1.467	1.569	1.714	1.631

correlated with an increase in the overall catalyst quantity. Consequently, 12CeNi@TS-1 demonstrated a significantly higher number of Ni NPs compared to the other catalysts. As detailed in Table 1, 12CeNi@TS-1 catalyst exhibited a higher quantity of Ni NPs interacting with the TS-1 relative to the other catalysts.

As illustrated in Fig. 2c, the Si 2p spectra of the six catalysts reveal the presence of Si-O signals. In comparison to pure TS-1 zeolite (103.22 eV), similar binding energies were observed for all six CeNi@TS-1 catalysts, indicating the formation of Ti-O-Si bonds.[63] Furthermore, with an increase in Ce content, a shift towards higher binding energy peaks was noted; this outcome suggests a subtle alteration in the chemical environment and implied the introduction of new species into the zeolite framework. This observation further reinforces the hypothesis that the CeO_2 was integrated into the zeolite structure.[62]

As presented in Figs.2d-h, ten distinct peaks were identified in the Ce spectra of the five CeNi@TS-1 catalysts. The analysis of the spin-orbit splitting of $3d_{5/2}$ and $3d_{3/2}$ revealed the presence of Ce^{4+} and Ce^{3+} species on the surfaces of these CeNi@TS-1 catalysts. For the Ce^{3+} species, four distinct signals were observed at 880.95 (V_1), 885.85 (V_2), 899.75 (V_3), and 905.05 eV (V_4). In contrast, six signals corresponding to the Ce^{4+} species were detected at 882.35, 888.15, 890.15, 902.05, 908.15, and 916.95 eV, which are designated as U_1-U_6, respectively.[63,64] It is noteworthy that the interaction between CeO_2 and the Ni NPs can facilitate the reduction of Ce^{4+} to Ce^{3+} through electron transfer.[64,65] As detailed in Table 2, the Ce^{3+} concentration on the surface was quantified using the molar ratio of $Ce^{3+}/Ce^{3+}+Ce^{4+}$. Comparison with Ni@TS-1, the Ce^{3+} concentration on the CeNi@TS-1 surface was markedly elevated. These peaks of Ce^{3+} are commonly regarded as indicators of OVs on the catalysts.[64,66] Furthermore, oxygen is typically found in a -2 oxidation state within metal oxides. To maintain charge balance, when oxygen atoms leave the surface, two electrons may be transferred to the metal ions, leading to the formation of OV defects or cations.[66] As reported in Table 2, a typical volcano curve was observed with increasing Ce concentration for the CeNi@TS-1 catalysts; this result aligns with the O 1s results shown in Fig. 2a. The maximum Ce^{3+} content of 51.1% was obtained for the 12CeNi@TS-1 catalyst, indicating significant formation of OVs within this catalyst. It is widely recognized that OVs play a crucial role in enhancing the CO_2 adsorption and activation, thereby facilitating the removal of carbon species generated from the CH_4 cleavage on the catalyst surface.[36,37] Moreover, CeO_2 possesses inherent basic properties that promote effective adsorption of CO_2 throughout the reaction process, subsequently aiding the gasification of carbonaceous species. Consequently, DRM catalysts with abundant OVs exhibit superior activity and stability, as exemplified by the remarkable 12CeNi@TS-1 catalyst prepared in this study.

Notably, a quartet of distinct signals was observed in the Ni 2p spectra presented in Figs. 2i-n for Ni-O-*X*, Ni^0, and Ni^{2+}, accompanied by a satellite peak.[67] The signal corresponding to Ni-O-*X* indicated a strong interaction between the Ni NPs and other constituents. Specifically, the Ni^0 signal suggested a weak interaction with the other system constituents and was associated with the relatively unencumbered Ni NPs. The presence of NiO species, resulting from the oxidation of metallic Ni in an atmospheric environment, manifested as a distinctive signal indicating the presence of Ni^{2+}. To elucidate the proportions of various constituents in the prepared catalysts, the molar ratios of $Ni^{2+}/Ni^{2+}+Ni^0+$Ni-O-*X*, Ni-O-*X*/$Ni^{2+}+Ni^0+$Ni-O-*X*, and $Ni^0/Ni^{2+}+Ni^0+$Ni-O-*X* were calculated, and the relevant values are displayed in Table 2. As the added CeO_2 amount increased, the Ni^{2+} and Ni-O-X percentages gradually rose, while the opposite trend was observed in the Ni^0 proportion. This can be primarily attributed to the incorporation of CeO_2, which led to a reduction the Ni NP size. Small Ni NPs are more prone to oxidation in air; consequently, the proportion of Ni^0 species was reduced and the prevalence of the NiO phase was enhanced. Simultaneously, the reduced Ni NP size enhanced their interactions with the other components, thereby increasing the proportion of Ni-O-*X* species. The theoretical value for Ni-O-*X* was measured at 852.60 eV, which is significantly lower than that observed for the Ni@TS-1 catalyst at 854.50 eV. This result suggests that the electrons of the Ni NPs were transferred to TS-1 via their interaction. In comparison with that of Ni@TS-1, the increasing CeO_2 contents of 3CeNi@TS-1, 6CeNi@TS-1, 9CeNi@TS-1, and 12CeNi@TS-1 resulted in a progressive blue shifting of the Ni-O-X signals, which indicates an enhanced interaction between the other components and Ni NPs.[68] When the CeO_2 content was further increased for 15CeNi@TS-1，a redshift in binding

energy was observed. This phenomenon can primarily be attributed to the generation of stronger Ni-O-*X* interactions by the small sized Ni NPs. These factors caused a more significant electron loss from the Ni NPs, which yielded more pronounced electron-deficient states. The Ni^{2+} signals of the prepared catalysts, which were located at 856.63 eV exceeded the standard value of 853.70 eV. Furthermore, a blue-shift trend was observed for the Ni^{2+} signal, which was attributed to factors similar to those mentioned above. Furthermore, the existence of OVs can also be confirmed through solid EPR spectroscopy. As illustrated in Fig. 2o, Ni@TS-1 and 12CeNi@TS-1 displays a pronounced and symmetrical Lorentzian line at g = 2.003, which indicates the presence of single electrons trapped by surface Ovs.[69,70] The intensity of characteristic peak for 12CeNi@TS-1 was markedly greater than that observed for Ni@TS-1, suggesting an elevated content of OVs in 12CeNi@TS-1. This observation further confirms the conclusions derived from the XPS analysis conducted on Ce 3d and O 1s.

3.3 Morphological analysis

3.3.1 SEM

Figs. 3a-h displays the SEM images of the TS-1 and CeNi/TS-1 catalysts. As illustrated in Fig. 3a, the pure TS-1 exhibits a morphology characterized by numerous irregular aggregates formed through the agglomeration of rectangular prisms and small particles, with a particle size range of 100-300 nm. In compared to the morphology of the pure TS-1, the incorporation of Ni and Ce into Ni/TS-1 and CeNi@TS-1 significantly altered the catalyst morphology after the "dissolution-recrystallization" process, as demonstrated in Figs. 3b-g. Notabley, a smoother surface textures and smaller in particle sizes were observed for these prepared catalysts. Furthermore, as illustrated in Fig. 3h and Figs. S3-S8, EDS analysis conducted on six different prepared catalysts revealed a relatively uniform distribution of elements including Si, O, Ti, Ni, and Ce. Additionally, the Ce concentration increased proportionally with the dosage, aligning with ICP analysis results.

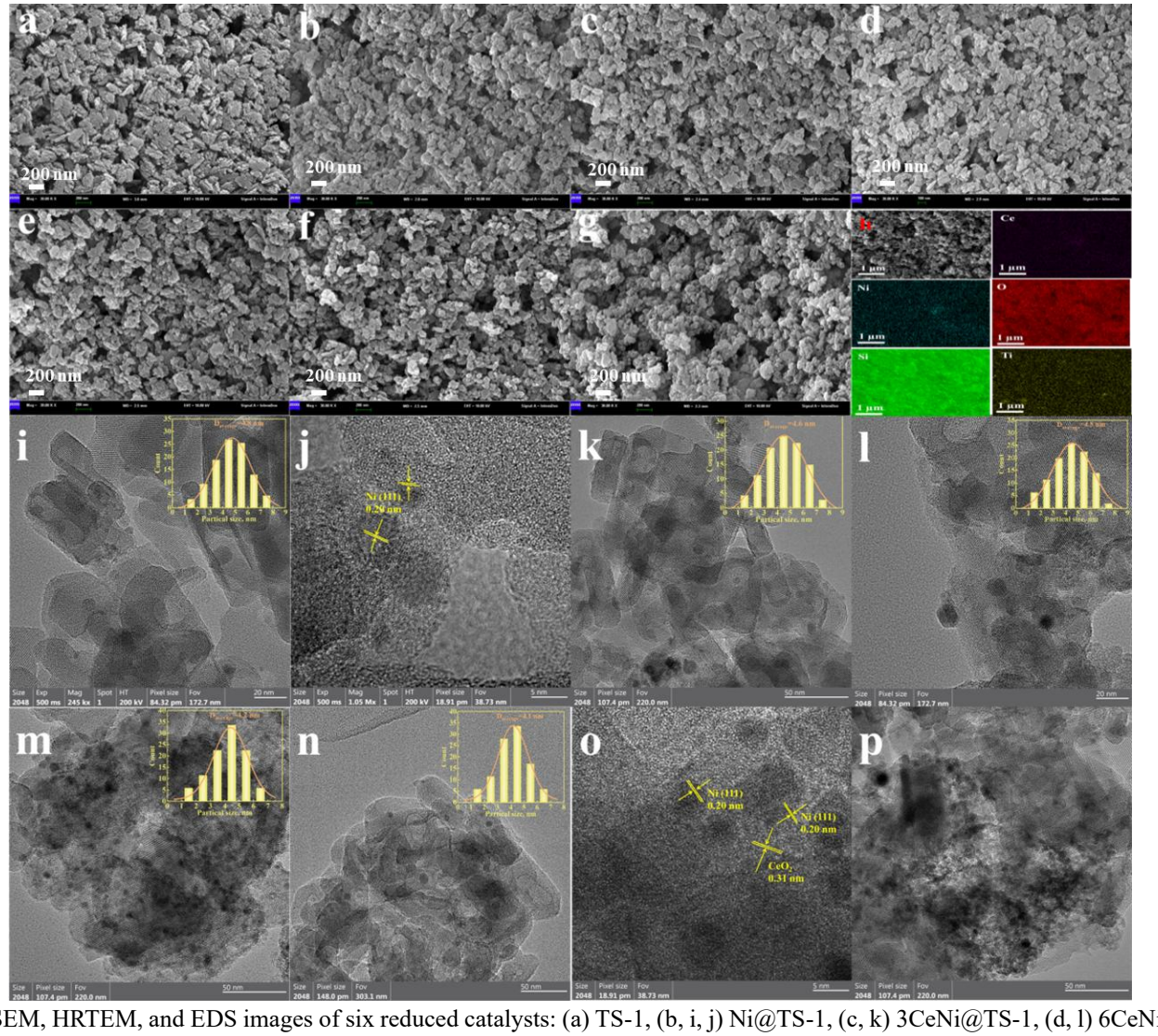

Fig. 3: SEM, HRTEM, and EDS images of six reduced catalysts: (a) TS-1, (b, i, j) Ni@TS-1, (c, k) 3CeNi@TS-1, (d, l) 6CeNi@TS-1, (e, m) 9CeNi@TS-1, (f, h, n, o) 12CeNi@TS-1, and (g, p) 15CeNi@TS-1.

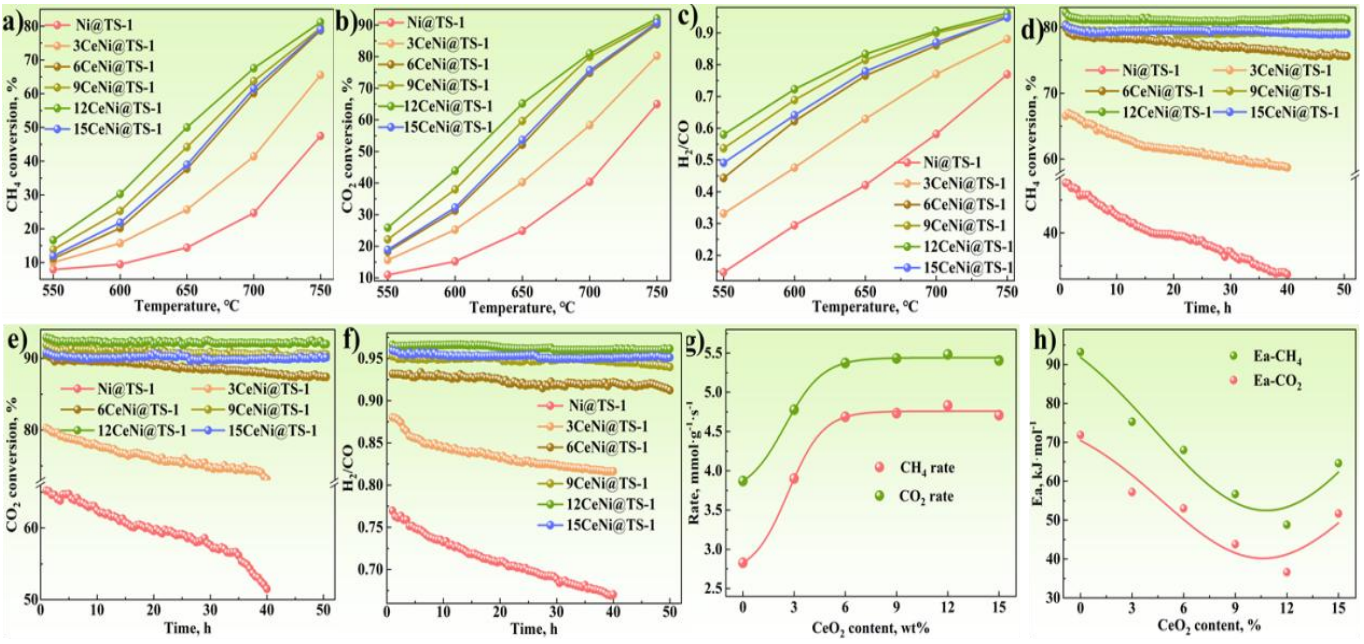

Fig. 4: CH_4 conversion rates (a), CO_2 conversion rates (b), and H_2/CO ratios (c) under different temperatures, and stability results for CH_4 conversion rate (d), CO_2 conversion rate (e), and H_2/CO ratio (f) for 50 h of DRM at 750 ºC for the CeNi@TS-1 catalysts. Correlation graphs of reaction rate (g) and activation energy E_a (h) with CeO_2 content. (reaction conditions: $CH_4/CO_2/N_2$= 4/4/2, GHSV= 60 $L \cdot g^{-1} \cdot h^{-1}$).

3.3.2 HRTEM

The HRTEM images of the series of CeNi@TS-1 catalysts and TS-1 are presented in Figs. 3i-p and Fig. S9. A characteristic agglomerated structure was observed for the pure TS-1, which is consistent with the SEM results (Fig. S9g). As the CeO_2 loading increased from 0 to 15%, the Ni NP size remained relatively stable at approximately 4-5 nm, with no significant CeO_2 agglomeration detected. This observation further corroborates the embedded structure for the CeNi@TS-1 catalyst, as opposed to a dispersed CeO_2 and Ni NPs on the surface.[43] The Ni@TS-1 catalyst consisted of TS-1 with embedded Ni NPs, as illustrated in Figs. 3i and 3j. The Ni NPs were evenly distributed throughout the TS-1. The size distribution of the metallic Ni NPs, which is statistically represented in Fig. 3i, was uniform, and the average diameter was 4.8 nm. The HRTEM image of Ni@TS-1 displayed in Fig. 3j reveals a measured lattice spacing of 0.20 nm, corresponding to the (111) plane of metallic Ni. In contrast, within the CeNi@TS-1 catalysts, there was a slight enhancement in the Ni dispersion due to embedded CeO_2 (Figs. 3k-p). As illustrated in Fig. 3o, for the 12CeNi@TS-1 catalyst, the lattice fringes measuring 0.31 and 0.20 nm correspond to CeO_2 (111) and Ni (111), respectively.[44] The metal Ni is in intimate contact with CeO_2, resulting in the formation of a closely-knit interfacial structure that enhances the support-metal interactions. Furthermore, their close proximity promotes improved adsorption and activation of CO_2 and CH_4 molecules at the OVs. For this catalyst, the average Ni NP size was calculated to be approximately 4.1 nm, which is slightly smaller than that of the Ni@TS-1. This indicates that the embedded CeO_2 facilitates the Ni NP dispersions via the substantial interactions.

3.4 Catalytic evaluation

The performance of the prepared CeNi@TS-1 catalysts for CH_4-CO_2 reforming was assessed at 550-750 ℃, under a GHSV of 60 $L \bullet g_{cat}^{-1} \bullet h^{-1}$ (N_2: CH_4: CO_2 = 2: 4: 4). As shown in Figs. 4a-c, the CH_4 and CO_2 conversion rates, as well as the H_2/CO ratios for prepared CeNi@TS-1 catalysts, exhibited an increasing trend with the temperature. Notable, the incorporation of CeO_2 resulted in significantly higher conversion rates for reactants on 12CeNi@TS-1 compared to those observed for Ni@TS-1. This enhancement can be attributed to the greater diversity and higher intensity of the Ni-O species, which led to a larger number of Ni NPs to exhibit pronounced electron deficiency states, more OVs, and an increased number of medium-strength basic sites. These factors facilitated CH_4 and CO_2 activation, thereby rendering this catalyst particularly suitable for DRM.[71,72] Within the examined temperature range, distinct trends were observed for the conversion rates of CH_4 and CO_2, along with the H_2/CO ratio: 12CeNi@TS-1> 9CeNi@TS-1> 15CeNi@TS-1> 6CeNi@TS-1> 3CeNi@TS-1> Ni@TS-1. The CO_2 conversion rate was slightly higher than that of CH_4 for the same catalyst; this can be attributed to the occurrence of a reverse water-gas shift reaction during the DRM process, resulting in a H_2/CO ratio of less than 1.00.[14,16] The composition of the catalyst suggests that the DRM performance improved rapidly a rapid increase from 0CeO_2 to 9CeO_2, and then rose slowly to 12CeO_2. A slight decline in performance was observed as 15CeO_2; the optimal peak was achieved with 12CeO_2. At 750 ℃, CH_4 and CO_2 conversion

rates of up to 91.2% and 92.3% were observed for 12CeNi@TS-1 catalyst, exceeding those of the reference catalyst Ni@TS-1 by approximately 1.71 and 1.42 times (47.5% and 65.0%, Fig. 4 and Fig. S10). As displayed in Fig. 4g, the CH_4 and CO_2 reaction rates increased in the following order: Ni@TS-1 (2.83 and 3.87 mmol·g_{Ni}^{-1}·s^{-1}) <3CeNi@TS-1 (3.90 and 4.78 mmol·g_{Ni}^{-1}·s^{-1}) <6CeNi@TS-1 (4.69 and 5.37 mmol·g_{Ni}^{-1}·s^{-1}) <15CeNi@TS-1 (4.70 and 5.40 mmol·g_{Ni}^{-1}·s^{-1}) <9CeNi@TS-1 (4.73 and 5.43 mmol·g_{Ni}^{-1}·s^{-1}) <12CeNi@TS-1 (4.83 and 5.48 mmol·g_{Ni}^{-1}·s^{-1}). Superior performance was observed for catalyst 12CeNi@TS-1. This outcome indicates that an increased CeO_2 content alters the Ni properties and spatial arrangement within the catalyst structure. This phenomenon can be attributed to its unique embedding architecture and distinctive electronic characteristics of Ce, which collectively enhance the active sites efficiency.

The conversion rates of CH_4 and CO_2 were measured for 12CeNi@TS-1, yielding values of 81.2% and 92.3%, respectively, with a H_2/CO ratio approaching 1 at 750 °C under a GHSV of 60 L•g_{cat}^{-1}•h^{-1} (Figs. 4d-f). Following a 50 h reaction time, the activity loss was recorded to be less than 1.0% (Table S1). In contrast, the Ni@TS-1 and 3CeNi@TS-1 catalysts exhibited rapid declines in both the CH_4 and CO_2 conversion rates, as well as H_2/CO ratio; notable, an activity loss exceeding 8% was observed after 20 h (Table S1, Figs. 4d-f). The observed deactivation discrepancy can likely be attributed to an imbalance between the "transient carbon" formation and elimination rates at the Ni NPs, which led to the carbon accumulation.[73] As the CeO_2 concentration continued to increase, the CH_4 and CO_2 conversion rates in the 6CeNi@TS-1 catalyst were markedly enhanced; this improvement was accompanied by a significant improvement in stability. However, the losses in CH_4 and CO_2 conversion rates and H_2/CO value were 4.2, 2.9, and 1.8% after a duration of 50 h, respectively. As the CeO_2 content of the 9CeNi@TS-1 catalyst was further increased, a slight enhancement in the CH_4 and CO_2 conversion rates was observed. A significant improvement in stability was noted, with the conversion rate losses remaining below 1%. Noted that, as the CeO_2 content increased to that of 12CeNi@TS-1, optimal levels were achieved for the catalytic activity and stability, with a conversion rate loss of less than 1%. However, upon increasing the CeO_2 content to 15CeNi@TS-1, minor decreases in both the activity and stability of the catalyst were noted, although the conversion rate loss of less than 1%. It should be emphasized that the acceptable carbon sources are contingent upon the CO disproportionation ($2CO^* \leftrightharpoons C^* + CO_2$) and/or the CH_4 dehydrogenation ($CH_4 \rightarrow H_2 + CH_x^*$; $CH_x^* \rightarrow H_2 + C^*$).[13,73,74] In this study, the presence of CeO_2 and OVs within the catalyst promoted the CO_2 and CH_4 conversion, while simultaneously facilitating the activation of reactive O* species for carbon removal. This interplay ultimately determined the catalyst resistance to carbon deposition.

To further analyze of the performance of the prepared CeNi@TS-1 catalysts, the apparent activation energy (E_a) of the DRM reaction was used to estimate the intrinsic activity of the prepared catalysts. As displayed in Fig. S10 and Fig. 4h, the CH_4 and CO_2 activation energies increased sequentially as follows: 12CeNi@TS-1 (48.8 and 36.6 kJ•mol^{-1}) <9CeNi@TS-1 (57.0 and 43.8 kJ•mol^{-1}) <15CeNi@TS-1 (64.6 and 51.7 kJ•mol^{-1}) <6CeNi@TS-1 (68.0 and 53.0 kJ•mol^{-1}) <3CeNi@TS-1 (75.3 and 57.2 kJ•mol^{-1}) <Ni@TS-1 (93.2 and 71.9 kJ•mol^{-1}). These results also align with the previous evaluation and analysis results. The differences in the CH_4 and CO_2 activation energies were as follows: 12CeNi@TS-1 (12.2 kJ•mol^{-1}) <15CeNi@TS-1 (12.9 kJ•mol^{-1}) <9CeNi@TS-1 (13.2 kJ•mol^{-1}) <6CeNi@TS-1 (15.0 kJ•mol^{-1}) <3CeNi@TS-1 (18.1 kJ•mol^{-1}) <Ni@TS-1 (21.3 kJ•mol^{-1}). Notably, the apparent E_a for CH_4 across all catalysts consistently exceeded that for CO_2, indicating that CH_4 activation was the rate-controlling step in the DRM process. The CH_4 activation energy exceeded that of CO_2 for all the CeNi@TS-1 catalysts, indicating that the coke formation may be more inclined towards the CO disproportionation rather than the CH_4 decomposition, which is insufficient for a dynamic carbon balance to be established. In contrast, the smallest difference in the E_a values of CH_4 and CO_2 (12.2 kJ•mol^{-1}) was observed for 12CeNi@TS-1 catalyst, indicating favorable reaction rate compatibility for the CH_4/CO_2 system (Fig. S10). This finding suggests that the "transient carbon" generated from the CH_4 decomposition can be swiftly eliminated by the active O* produced through CO_2 dissociation at OVs. This mechanism facilitates the DRM reaction, aligning with the stability structures illustrated in Figs. 4d-f.

3.5 Characterization of used catalysts

Figs. 5a-g and Fig. S11 present TEM images of the used catalysts, demonstrating that the original morphology of TS-1 zeolite nano-layers was preserved. A significant accumulation of whisker-like carbon deposits was observed on the catalyst surface of the Ni@TS-1; these deposits were primarily responsible for the deactivation of this catalyst. A small amount of whisker-like carbon was evident in 3CeNi@TS-1. Note that the continuous growth of carbon whiskers obstructs the catalyst pores. When substantial chunks of coke are forced into the pore walls of the compressed support, their mechanical strength of these chunks significantly exceeds that of the support material. This ultimately leads to the collapse of catalyst pores, resulting in irreversibly damage to the catalyst and rapid deactivation.[74] Notably, increased CeO_2 content (6CeNi@TS-1, 9CeNi@TS-1, 12CeNi@TS-1, and 15CeNi@TS-1) significantly reduced in the formation of the whisker-like deposited carbon; this is the primary reason for the enhanced stability observed for those catalysts. In particularly, no carbon deposition was observed for 12CeNi@TS-1, as shown Figs. 5e and 5f. Furthermore, after operation at temperatures exceeding 750 °C for 50 h, the Ni NPs remained well-dispersed (Fig. 5e). However, their average size increased to approximately 7.7 nm. This result

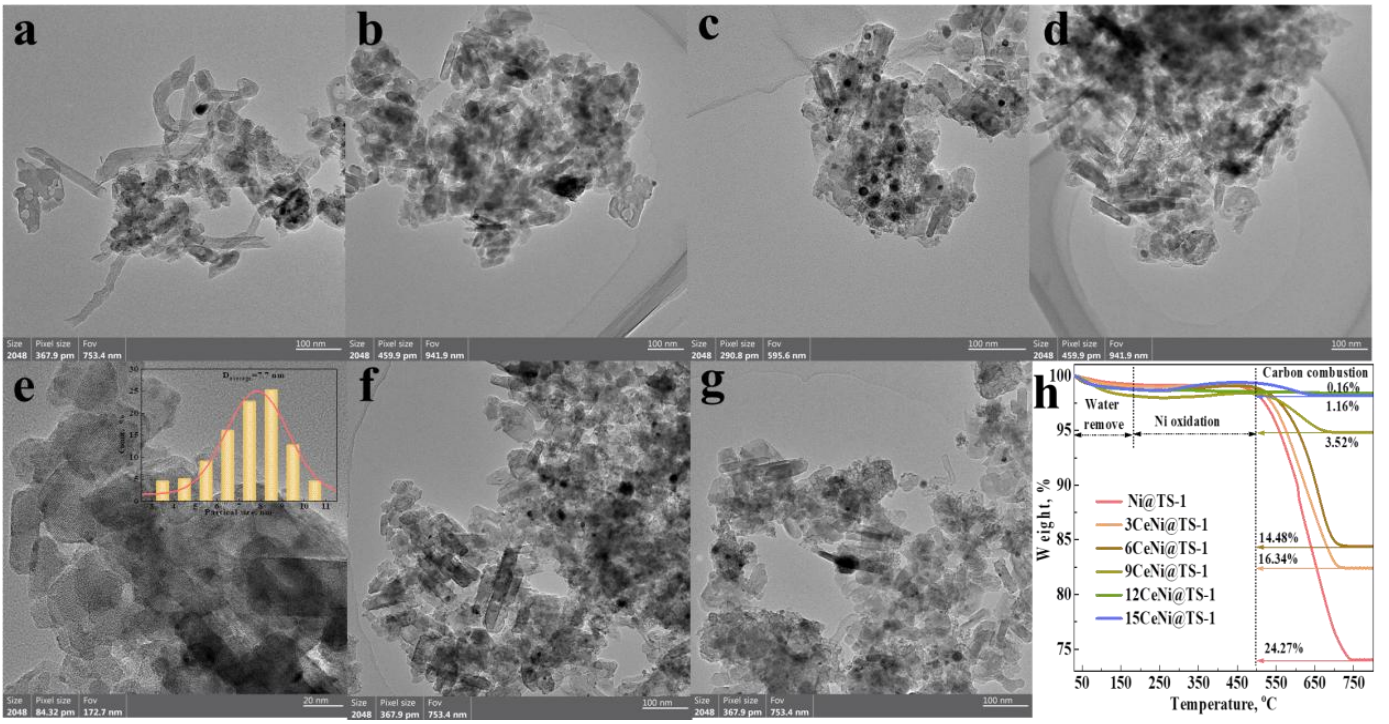

Fig. 5: TEM images (a-g) and TG profiles (h) of used catalysts after 50 h: (a) Ni@TS-1, (b) 3CeNi@TS-1, (c) 6CeNi@TS-1, (d) 9CeNi@TS-1, (e, f) 12CeNi@TS-1, and (g) 15CeNi@TS-1.

indicates that confinement of Ce and Ni nanoparticles within the TS-1 zeolite matrix enhances the sintering resistance, thereby contributing to improved catalytic stability.

The TG profiles of the spent catalysts (Fig. 5h) indicated a weight reduction occurring at temperatures of less 185 °C, which was attributed to desorption of the adsorbed water upon exposure to air.[75] In the range of 185-495 °C, a weight increase was observed, attributed to the oxidation of the Ni metal. For the six spent catalysts, the weights consistently remained below 1.0%. The enhancement observed for each sample was less than the theoretical value, indicating that the Ni NPs underwent partial oxidation prior to the TG analysis. At temperatures exceeding 495 °C, the observed weight loss was primarily attributed to the combustion of carbon deposits.[75] Analysis of the declining curves revealed that the extent of carbon deposition on the used catalysts followed the order: Ni@TS-1 (24.27%) >3CeNi@TS-1 (16.34%) >6CeNi@TS-1 (14.48%) >9CeNi@TS-1 (3.52%) >15CeNi@TS-1 (1.16%) >12CeNi@TS-1 (1.16%), which is consistent with the previous analytical results. Furthermore, in the CeNi@TS-1 catalysts, the carbon species exhibited an initial decrease followed by an increase with the addition of CeO_2, owing to changes in the medium-strength basic sites.[76] Additionally, the redox cycle between Ce^{3+} and Ce^{4+} along with the presence of OVs, positively influences the catalyst resistance against coking. The initial increase in the Ce^{3+} ion concentration, followed by a subsequent decrease, further elucidates this observation. Therefore, only the optimal amount of CeO_2 enables the catalyst to exhibit excellent anti-coking performance.

3.6 In-situ DRIFTS

The investigation of DRM using Ni@TS-1 and 12CeNi@TS-1 catalysts was conducted through In-Situ DRIFTS. As illustrated in Figs. 6a and 6b, this analysis provided significant insights into the surface dynamics and elucidated the role of CeO_2 throughout the DRM within the reaction pathway. The species variations on the catalyst surface were systematically examined via a controlled heating process, with temperatures from 50 to 500 °C. As the temperature increased, gradual decreases in the signal intensities at approximately 3015 (gaseous CH_4), 2357, and 2345 cm^{-1} (gaseous CO_2) were observed for both the Ni@TS-1 and 12CeNi@TS-1. This trend was particularly pronounced for the catalyst 12CeNi@TS-1, further supporting the hypothesis that elevated temperatures facilitate this reaction in accordance with its thermodynamic characteristics. These preliminary findings indicate exceptional performance for the 12CeNi@TS-1 catalyst. The peak observed at 2307 cm^{-1}, corresponding to gasphase CO on Ni@TS-1, was first detected at 300 °C, suggesting the onset of the DRM reaction. In contrast, for 12CeNi@TS-1, this distinct signal first appeared at a significantly lower temperature of 175 °C, thereby demonstrating superior catalytic performance compared to Ni@TS-1. The peak observed at 2085 cm^{-1}, corresponding to linearly coordinated CO species on metallic Ni sites of Ni@TS-1, gradually intensified. This enhancement can be ascribed to the increased quantity of CO linear species as the DRM reaction progressed. It is noteworthy that desorption from metallic Ni is challenging for these species.[63,77] In contrast, for 12CeNi@TS-1, this signal remained relatively

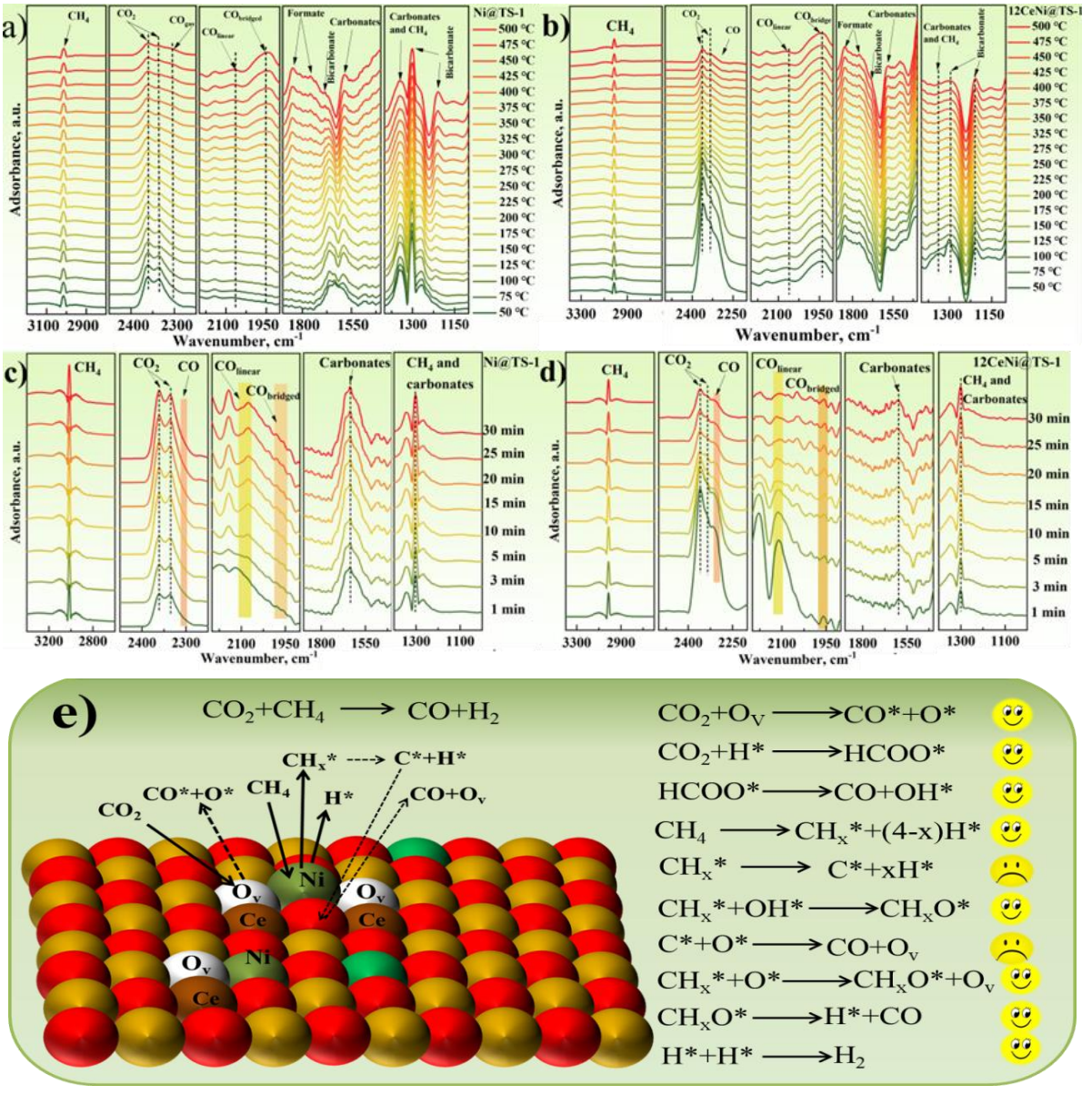

Fig. 6: In-situ DRIFTS measurement results for Ni@TS-1 and 12CeNi@TS-1 catalysts: (a,b) a temperature increase from 50 to 500 °C, (c,d) a constant temperature of 500 °C for 30 min, and (e) schematic of the potential DRM reaction pathway over 12CeNi@TS-1.

stable, indicating that the linear CO species were more readily desorbed from this catalyst. Furthermore, both catalysts exhibited gradual increases in the signal observed at 1948 cm^{-1}, which corresponds to bridging of the CO species. These observations suggest progressive amplification of the DRM process. Consequently, it can be deduced that the linear CO species may serve as a key intermediate.[77,78] Notably, for 12CeNi@TS-1, the peak associated with bridging CO species was more pronounced; this result further evidences the higher activity of this catalyst. Gradual intensification of the peaks observed at 1843 and 1746 cm^{-1} was observed for both catalysts; these peaks are attributed to formate species, with more pronounced peaks detected for 12CeNi@TS-1. This enhancement is attributed to the increased CH_4 and CO_2 activation. A similar phenomenon is observed for the signals at 1586 cm^{-1}, which corresponds to the carbonate species. This observation further indicates a gradual intensification of CO_2 activation process. For the Ni@TS-1 catalyst, the intensity of the signal at 1686 cm^{-1}, associated with bicarbonate species, progressively decreased among the intermediate signals corresponding to the formate and carbonate species. This reduction can be ascribed to the decomposition of the bicarbonate species into formate and carbonate at elevated temperatures. In contrast, for 12CeNi@TS-1, this signal peak was diminished; this reduction may have been due to a rapid conversion of the formate and carbonate species into other entities within the catalytic system. As the DRM proceeded vigorously, ultimately, even the bicarbonate signal disappeared (Fig. 6b). According to literature.[77,78] formates and carbonates play crucial roles as surface-active

intermediates in the activation of CO_2 and CH_4. The peaks observed at 1312 cm^{-1}, attributed to both carbonate and gas-phase CH_4 species, can be interpreted as a mixture of these two components due to the overlapping characteristic signals. Slight differences in the signals of the two catalysts were observed. For Ni@TS-1, the peak was particularly pronounced, and the trend was characterized by an initial decrease followed by a stabilization phase. In contrast, the peak for 12CeNi@TS-1 faded quickly after its initial appearance. This phenomenon can be attributed to the fact that higher CH_4 consumption compared to the carbonate species produced at the lower temperatures was observed for Ni@TS-1, conversion of the generated carbonate being facilitated. Furthermore, notable differences were observed in the peaks at 1191 and 1285 cm^{-1} for both catalysts, which correspond to the bicarbonate species. For Ni@TS-1, the peak at 1285 cm^{-1} exhibited a gradually decrease and subsequently stabilized, while the peak at 1191 cm^{-1} showed a progressively increase before reaching stable. For 12CeNi@TS-1, rapid stabilization following reduction was observed for the distinctive peaks at 1285 and 1191 cm^{-1}; however, the peak intensities were significantly lower than those of Ni@TS-1. For both catalysts, a gradual weakening of the peak was observed for the peaks at 1686 cm^{-1}, which correspond to bicarbonate species; more pronounced was observed for the peaks of 12CeNi@TS-1. Note that the peak observed at 1336 cm^{-1}, which corresponds to gaseous CH_4 and carbonate species, was regarded as a composite of these components because of the overlap of their characteristic signals. Notably, for Ni@TS-1, an initial decrease was observed for this signal, followed by a subsequent increase. This behavior can be attributed to the fact that under low-temperature conditions, the methane consumption exceeds the carbonate species production; conversely, under high-temperature conditions, the opposite trend is evident. Importantly, for 12CeNi@TS-1, this signal rapidly disappeared after its appearance at low temperatures. This behavior may indicate rapid conversion of the generated carbonate species. Furthermore, similar trends were observed for both Ni@TS-1 and 12CeNi@TS-1 catalysts; specifically, there was a gradual enhancement of their respective peaks at 1191 and 1285 cm^{-1} (bicarbonate), as well as for their peak at 1686 cm^{-1} (bicarbonate).

As shown in Figs. 6c and 6d, the two catalysts were evaluated at a constant temperature of 500 ℃, with each testing period lasting for 30 min. At 300 ℃, both catalysts have already demonstrated their ability to initiate the DRM reaction. Note that an increase in temperature may not significantly alter the reaction pathway; rather, temperature increases predominantly accelerate the reaction rate. Consequently, 500 ℃ is considered suitable for the examination of surface reactions.

For both the Ni@TS-1 and 12CeNi@TS-1 catalysts, no significant changes over time were observed for the peaks of gaseous CO, CO_2, and CH_4 after a duration of 10 min. This observation indicates that the stable equilibrium state was achieved for the DRM reaction at this time point. In this stable equilibrium state, valuable insights for surface processes were obtained through the analysis of specific intermediate signals, elucidating the role of CeO_2 within the DRM pathway of 12CeNi@TS-1. In contrast to Ni@TS-1, the peak corresponding to the linear CO species continued to intensify over time, the peak for the bridged CO species was not detectable because of its lower desorption energy; this suggests that the linear CO molecules may serve as pivotal surface-active intermediates. For 12CeNi@TS-1, however, the linear CO peak gradually diminished over time and ultimately disappeared. This observation indicates that the linear CO is more susceptible to desorption, thereby facilitating the primary reaction and mitigating the formation of carbon species resulting from CO disproportionation.[76,78] Furthermore, no signal peaks corresponding to formate species were detected in either catalyst, whereas signal peaks for carbonate species were distinctly observed; these peaks indicated considerable stability. Notably, for 12CeNi@TS-1, the signal peak for the carbonate species was relatively weak; this may have been attributed to the capacity of the catalyst for the rapid conversion of carbonate species.

According to the literature,[29,68] and the results from in-situ DRIFTS, the potential mechanisms underlying the adsorption, CO_2 and CH_4 activation and conversion during the DRM reaction for 12CeNi@TS-1 catalyst can be delineated as follows (Fig. 6e). The abundant VOs generated during the "impregnation-recrystallization" of the 12CeNi@TS-1 sample played a pivotal role in facilitating both CH_4 and CO_2 activation. As reactants, the CO_2 were adsorbed onto the medium-strength basic sites, while CH_4 molecules interacted with Ni NPs, respectively. CO_2 was activated at the OVs before, ultimately transforming into the active O atoms and CO products. These active O atom species were drawn to neighbouring OVs, where they engaged in the CH_4 activation and transformation. Concurrently, the metallic Ni NPs, which were characterized by the elevated surface charge density, facilitated the activation of the initial C-H bond of the adsorbed CH_4 molecules. This interaction prompted a dissociation process, yielding H and CH_3 species that subsequently engage in bonding with the Ni metal. Later, the CH_3 species adsorbed on the Ni NPs of the TS-1 were transferred to the adjacent lattice oxygen atoms, leading to the formation of CH_xO species. Ultimately, CO was generated through the dehydrogenation reaction of the CH_xO species, during which the active H atoms converged to form H_2. Additionally, the OVs were also conceived during this pivotal phase.

4. Conclusion

The methane dry reforming process (DRM) is an upstream reaction within the chemical product synthesis chain, facilitating the conversion of carbon dioxide (CO_2) and methane (CH_4)-two major greenhouse gases-into synthesis gas (H_2/CO). By precisely controlling the H_2/CO ratio, this

process can be further utilized in carbonylation or Fischer-Tropsch reaction, thereby enabling the production of various fuels through downstream processes. In this work, a series of CeNi@TS-1 catalysts was carefully synthesized using the co-impregnation-recrystallization method, with TS-1 zeolite serving as a support. The prepared catalysts were employed in the DRM reaction, and their catalytic performance was tested at 550-750 ℃ with a GHSV of 60 $L \cdot g^{-1} \cdot h^{-1}$. Among the evaluated catalysts, exceptional activity was observed for 12CeNi@TS-1, achieving conversions of 81.2% for CH_4 and 92.3% for CO_2. After 50 h, the H_2/CO ratio remained stable at 0.96, with only minor activity losses recorded for CH_4 and CO_2 at 0.2% and 0.3%, respectively. This indicates robust stability. Overall, CeO_2 incorporation enhanced the interaction between the other components (CeO_2 and TS-1) and Ni nanoparticles (NPs) through recrystallization; specifically, it resulted in reduced Ni NP sizes while increasing the number of oxygen vacancy (OV) environments. Consequently, these Ni NPs exhibited stronger electron-deficient states that not only favoured the CH_4 and CO_2 activation but also improved the catalyst stability. Notably, excess CeO_2 may obscure some Ni NPs, thereby hindering access to active sites, which is detrimental to the DRM. Therefore, it is essential that the Ni@TS-1 catalyst contains an appropriate amount of CeO_2 for remarkable catalytic efficacy to be achieved. Further, the CeO_2 embedded on the catalyst not only facilitates full activation of CH_4 and CO_2 but also accelerates the dissociation of CO. This approach mitigates CH_4 cracking while enhancing both the catalytic performance and stability. Moreover, this present work presents a novel strategy for Ni based catalysts with rich OVs, as well as a new approach for developing of high-temperature resistant Ni-based catalysts that mitigate sintering. Therefore, the strategic incorporation of Ce into Ni-based catalysts through confinement effects can significantly enhance the oxygen supply mechanism, thereby facilitating the gasification of deposited carbon. This work provieds a valuable insight for the industrialization of processes related to CO_2 capture, storage and utilization, in addition to chemical chain reactions involving CH_4.

Acknowledgements

The authors would like to express their sincere gratitude for the funding from the National Natural Science Foundation of China (22272086), Natural Science Foundation of Sichuan Province (2023NSFSC0009, 2023NSFSC0096), Key Laboratory of Green Catalysis of Higher Education Institutes of Sichuan (LYJ2403), Sichuan Technology & Engineering Research Center for VanadiumTitanium Materials (2021-FTGC-YB-06), and the Innovation and Entrepreneurship Training Program for Undergraduates in Sichuan Province (S202411360048).

Conflict of Interest

There is no conflict of interest.

Supporting Information

Applicable.

CRediT Statement

Huabing Zhang: Data curation, Data visualization, Methodology, Formal analysis, Writing – original draft. **Dandan Sun:** Formal analysis, Methodology. **Xinyue Zhang:** Data curation, Methodology. **Jin He:** Data curation, Formal analysis. **Houxiang Sun:** Resources, Funding acquisition, Writing – review & editing. **Haiyan Yang: Zhiqiang Jiang:** Resources, Funding acquisition, Writing – review & editing. **Yani Liu:** Supervision, Methodology. **Furong Li:** Supervision, Formal analysis. **Wenwu Zhou:** Resources, Funding acquisition, Writing – review & editing.

References

[1] Y. Song, E. Ozdemir, S. Ramesh, A. Adishev, S. Subramanian, A. Harale, M. Albuali, B.A. Fadhel, A. Jamal, D. Moon, S.H. Choi, C.T. Yavuz, Dry reforming of methane by stable Ni-Mo nanocatalysts on single-crystalline MgO, *Science*, 2020, **367**, 777–781, doi: 10.1126/science.aav2412.

[2] Z. Du, F. Chen, S. Fang, X. Yang, Y. Ge, K. Shurtz, H.C. Zhou, Y. H. Hu, Y. Li, Engineering Bimetallic Ni-Cu Nanoparticles Confined in MOF-Derived Nanocomposite for Efficient Dry Reforming of Methane, *ES Energy & Environment*, 2024, **23**, 1097, doi: 10.30919/esee1097.

[3] B. A. Thirumalarasu, A. Rajagopalan, S. Murugan, U. B. R. Ragula, Direct conversion of biogas to syngas over bimetallic nickel–cobalt supported on α-alumina catalysts, *Renewable Energy*, 2024, **234**, 121200, doi: 10.1016/j.renene.2024.121200.

[4] A. M. Alhassan, I. Hussain, O. A. Taialla, M. M. Awad, A. Tanimu, K. Alhooshani, S. A. Ganiyu, Advances in catalytic dry reforming of methane (DRM): Emerging trends, current challenges, and future perspectives, *Journal of Cleaner Product*, 2023, **423**, 138638, doi: 10.1016/j.jclepro.2023.138638.

[5] Z. Niu, P. Han, Y. Du, Z. Han, L. Lang, X. Li, X. Yin, Ni-La confined in TiO_2 nanotubes with efficient activity and stability for dry methane reforming, *Renewable Energy*, 2025, **248,** 123150, doi: 10.1016/j.renene.2025.123150.

[6] X. Ma, W. W. Yang, J. W. Su, L. X. Liang, W. X. Yang, Y. L. He, Enhancing carbon dioxide conversion in methane dry reforming multistep reactions through transformation of active species on catalyst surface, *Energy*, 2024, **290**, 130279, doi: 10.1016/j.energy.2024.130279

[7] H. Wu, Y. Li, H. Liu, D. He, High-pressure Catalytic Kinetics of CO_2 Reforming of Methane Over Highly Stable NiCo/SBA-15 Catalyst, *ES Energy & Environment*, 2019, **3**, 67-73, doi: 10.30919/esee8c201.

[8] Y. Zhang, S. Li, Y. Fu, L. Zheng, H. Li, W. Kong, B. Pan, J. Li, J. Zhang, Y. Sun, Local coordination environment triggers key Ni-O-Si copolymerization on silicalite-2 for dry reforming of methane, *Applied Catalysis B-Environmental and Energy*, 2024, **350**, 123903, doi: 10.1016/j.apcatb.2024.123903.

[9] R. Colombo, G. Moroni, C. Negri, G. Delen, M. Monai, A.

Donazzi, B. M. Weckhuysen, M. Maestri, Surface carbon formation and its impact on methane dry reforming kinetics on rhodium-based catalysts by operando Raman spectroscopy, *Angewandte Chemie International Edition*, 2024, **63**, e202408668. doi: 10.1002/anie.202408668.

[10] D. Wang, P. Littlewood, T. J. Marks, P. C. Stair, E. Weitz, Coking can enhance product yields in the dry reforming of methane, *ACS Catalysis*, 2022, **12**, 8352–8362, doi: 10.1021/acscatal.2c02045.

[11] A. A. Khan, M. Tahir, N. Khan, Process optimization and kinetic study for solar-driven photocatalytic methane bi-reforming over TiO_2/Ti_3C_2 supported CoAlLa-LDH-g-C_3N_4 dual S-scheme nanocomposite, *Energy Conversion and Management*, 2023, **286**, 17021, doi: 10.1016/j.enconman.2023.117021.

[12] J. Yu, T. Le, D. Jing, E. Stavitski, N. Hunter, K. Lalit, D. Leshchev, D. E. Resasco, E. H. Sargent, B. Wang, W. Huang, Balancing elementary steps enables coke-free dry reforming of methane, *Nature Communications*, 2023, **14**, 7514, doi: 10.1038/s41467-023-43277-0.

[13] A. Abdulrasheed, A. A. Jalil, Y. Gambo, M. Ibrahim, H. U. Hambali, M. Y. Shahul Hamid, A review on catalyst development for dry reforming of methane to syngas: Recent advances, *Renewable Sustainable Energy Reviews*, 2019, **108**, 175-193, doi: 10.1016/j.rser.2019.03.054.

[14] Y. Wei, W. Cai, S. Deng, Z. Li, H. Yu, S. Zhang, Z. Yu, L. Cui, F. Qu, Efficient syngas production via dry reforming of renewable ethanol over Ni/KIT-6 nanocatalysts, *Renewable Energy*, 2020, **145**, 1507-1516, doi: 10.1016/j.renene.2019.07.077.

[15] I. Salahshoori, M. N. Jorabchi, M. Asghari, S. Wohlra, M. Golriz, H. A. Khonakdar, Comprehensive insights into molecular simulation-driven advances in functional materials for pollutant mitigation, *Coordination Chemistry Reviews*, 2025, **534**, 216580, doi: 10.1016/j.ccr.2025.216580.

[16] H. Sun, L. Li, H. Zhang, H. Yang, T. Yang, M. Shu, Z. Zhong, M. Yi, B. Meng, Effect of Zirconium modified Y zeolite via in situ synthesis and its regulation on the formation of excellent NiW catalyst for ultra-deep hydrodesulfurization of 4,6-DMDBT, *Chemical Engineering Journal*, 2023, **478**, 147514, doi: 10.1016/j.cej.2023.147514.

[17] Z. Dong, E. Zhang, Y. Jiang, Q. Zhang, A. Mayoral, H. Jiang, Y. Ma, Atomic-Level Imaging of Zeolite Local Structures Using Electron Ptychography, *Journal of the American Chemical Society*, 2023, **145**, 6628-6632, doi: 10.1021/jacs.2c12673.

[18] J. Chen, Y. Zhu, W. Li, F. Luo, S. Li, X. Li, Y. Huang, A. Zhang, Z. Xiao, D. Wang, Z. Zheng, Production of diesel-like hydrocarbons via hydrodeoxygenation of palmitic acid over Ni/TS-1 catalyst. *Biomass Bioenergy*, 2021, **149**, 106081, doi: 10.1016/j.biombioe.2021.106081.

[19] Y. Zhu, J. Chen, W. Li, D. Wang, S. Li, Z. Zheng, A new method for long-chain alkanes under a condition without extra hydrogen source: Catalytic upgrading of cellulose pyrolysis vapors over Au/TS-1 catalyst, *Journal of Analytical Applied Pyrolysis*, 2020, **151**, 104906, doi: 10.1016/j.jaap.2020.104906.

[20] W. Hou, K. Lin, X. Zhang, B. Xu, Y. Wang, X. Lu, Y. Gao, R. Ma, Y. Fu, W. Zhu, Highly stable and selective Pt/TS-1 catalysts for the efficient nonoxidative dehydrogenation of propane, *Chemical Engineering Journal,* 2023, **474**, 145648, doi: 10.1016/j.cej.2023.145648.

[21] Y. Wei, G. Li, R. Su, H. Lu, H. Guo, Ti-sites environment-mediated hierarchical TS-1 catalyzing the solvent-free epoxidation: The remarkably promoting role of alcohol modification, *Applied Catalysis A, General*, 2019, **582**, 117108, doi: 10.1016/j.apcata.2019.06.006.

[22] Y. Pan, A. Bhowmick, W. Wu, Y. Zhang, Y. Diao, A. Zheng, C. Zhang, R. Xie, Z. Liu, J. Meng, D. Liu, Titanium silicalite-1 nanosheet-supported platinum for nonoxidative ethane dehydrogenation, *ACS Catalysis*, 2021, **11**, 9970–9985, doi: 10.1021/acscatal.1c02676.

[23] X. Tao, F. Yu, P. Yu, H. Yu, T. Zhao, M. Li, H. Wang, Local coordination configuration of Ni and Co in $MgAl_2O_4$ spinel structure and the performance of NiCo/MgO-Al_2O_3 catalyst for dry reforming of methane, *Chemical Engineering Journal,* 2025, **507**, 160708, doi: 10.1016/j.cej.2025.160708.

[24] A. Jamsaz, N. Pham-Ngoc, M. Wang, D. H. Jeong, E. S. Oh, E.W. Shin, Synergistic effect of macroporosity and crystallinity on catalyst deactivation behavior over macroporous Ni/$Ce_xZr_{1-x}O_2$-Al_2O_3 for dry reforming of methane, *Chemical Engineering Journal,* 2023, **476**, 146821, doi: 10.1016/j.cej.2023.146821.

[25] Y. Fu, W. Kong, B. Pan, C. Yuan, S. Li, H. Zhu, J. Zhang, Boron-promoted Ni/MgO catalysts for enhanced activity and coke suppression during dry reforming of methane, *Journal of the Energy Institute*, 2022, **105**, 214–220, doi: 10.1016/j.joei.2022.09.005.

[26] M. Kushida, A. Yamaguchi, M. Miyauchi, Photocatalytic dry reforming of methane by rhodium supported monoclinic TiO_2-B nanobelts, *Journal of Energy Chemistry*, 2022, **71**, 562–571, doi: 10.1016/j.jechem.2022.04.022.

[27] H. Jiao, G. C.Wang, A Comprehensive Theoretical Study of the Mechanism for Dry Reforming of Methane on a $Ni_4/ZrO_2(101)$ Catalyst Under External Electric Fields: The Role of Interface and Oxygen Vacancy, *ACS Catalysis*, 2025, **15**, 3846–3859, doi: 10.1021/acscatal.4c05758.

[28] J. Liu, H. Sun, S. H. Hu, B. Hu, Z. M. Fang, J. Li, Z. Zhang, Q. Lu, Hydrogen production from the steam reforming of biogas over Ni-based catalyst: The role of promoters and supports, *Energy*, 2024, 311, 133480, doi: 10.1016/j.energy.2024.133480.

[29] H. C. Wu, T. C. Chen, J. H. Wu, C. W. Pao, C. S. Chen, Influence of sodium-modified Ni/SiO_2 catalysts on the tunable selectivity of CO_2 hydrogenation: Effect of the CH_4 selectivity, reaction pathway and mechanism on the catalytic reaction, *Journal of Colloid and Interface Science*, 2021, **586**, 514-527, doi: 10.1016/j.jcis.2020.10.117.

[30] S. Das, J. Ashok, Z. Bian, N. Dewangan, M. H. Wai, Y. Du, A. Borgna, K. Hidajat, S. Kawi, Silica-Ceria sandwiched Ni core-shell catalyst for low temperature dry reforming of biogas: Coke resistance and mechanistic insights, *Applied Catalysis B: Environmental* 2018, **230**, 220–236, doi: 10.1016/j.apcatb.2018.02.041.

[31] G. Li, H. Hao, P. Jin, M. Wang, Y. Yu, C. Zhang, Dry

reforming of methane over Ni/Al_2O_3 catalysts: Support morphological effect on the coke resistance, *Fuel*, 2024, **362**, 130855, doi: 10.1016/j.fuel.2024.130855.
[32] M. Usman, W.M.A. Wan Daud, H.F. Abbas, Dry reforming of methane: Influence of process parameters-A review, *Renewable Sustainable Energy Reviews*, 2015, **45**, 710–744, doi: 10.1007/s13399-019-00417-1.
[33] Y. H. Wang, H. M. Liu, B. Q. Xu, Durable Ni/MgO catalysts for CO_2 reforming of methane: Activity and metal-support interaction, *Journal of Molecular Catalysis A: Chemical*, 2009, **299**, 44–52, doi: 10.1016/j.molcata.2008.09.025.
[34] A. F. Lucrédio, J. M. Assaf, E. M. Assaf, Methane conversion reactions on Ni catalysts promoted with Rh: Influence of support, *Applied Catalysis A, General*, 2011, **400**, 156–165, doi: 10.1016/j.apcata.2011.04.035.
[35] B. Han, Y. Wang, Z. Huang, Z. Zhang, T. Tan, J. Xie, Y. Chen, Sol-gel synthesis of Pt-Co-CeO_x codierite catalyst for biogas reforming to methanol compatible syngas, *Energy*, 2025, **329**, 136707, dio: 10.1016/j.energy.2025.136707.
[36] Y. Li, Z. Li, N. Wang, Y. Zha, K. Zheng, Y. Xu, B. Liu, X. Liu, Strong activity-based volcano-type relationship for dry reforming of methane through modulating Ni-CeO_2 interaction over Ni/CeO_2-SiO_2 catalysts, *Chemical Catalysis*, 2025, **5**, 101189, doi: 10.1016/j.checat.2024.101189.
[37] O. Tammaro, R. Paparo, M. Chianese, I. Ritacco, L. Caporaso, M.F. Camellone, B. Masenelli, A. D. Lamirand, J. M. Bluet, M. Fontana, G. Pinto, A. Illiano, A. Amoresano, M. D. Serio, V. Russo, S. Esposito, Reverse micelle strategy for effective substitutional Fe-doping in small-sized CeO_2 nanocrystals: Assessment of adsorption and photodegradation efficiency of ibuprofen under visible light, *Chemical Engeering Journal*, 2024, **479**, 147909, doi: 10.1016/j.cej.2023.147909.
[38] L. Luisetto, S. Tuti, C. Romano, M. Boaro, E. Di Bartolomeo, J. K. Kesavan, S. S. Kumar, K. Selvakumar, Dry reforming of methane over Ni supported on doped CeO_2: New insight on the role of dopants for CO_2 activation, *J CO_2 Utilization*, 2019, **30**, 63–78, doi: 10.1016/j.jcou.2019.01.006.
[39] D. Guo, Y. Lu, Y. Ruan, Y. Zhao, Y. Zhao, S. Wang, X. Ma, Effects of extrinsic defects originating from the interfacial reaction of CeO_{2-x}-nickel silicate on catalytic performance in methane dry reforming, *Applied Catalysis B: Environmental*, 2020, **277**, 119278, doi: 10.1016/j.apcatb.2020.119278.
[40] Z, Bian, Y. M. Chan, Y. Yu, S. Kawi, Morphology dependence of catalytic properties of Ni/CeO_2 for CO_2 methanation: A kinetic and mechanism study, *Catalysis Today*, 2020, **347**, 31–38, doi: 10.1016/j.cattod.2018.04.067.
[41] D. Zhou, H. Huang, W. Liang, X. Wu, C. Dang, W. Cai, Balancing the carbon formation and removal by regulating Zr doping within CeO_2 nanotube-supported-Ni catalysts for deriving the superior stability in low-temperature dry reforming of methane, *Energy Conversion and Managent*, 2024, **322**, 119140, doi: 10.1016/j.enconman.2024.119140.
[42] R. Amin, X. Chang, B. Liu, Synergistic effect of CeO_2 in CH_4/CO_2 dry reforming reaction over stable xCeO_2yNi/MCM-22 catalysts, *Industrial Engineering Chemistry Research*, 2017, **56**, 7445–7453, doi: 10.1021/acs.iecr.7b01375.
[43] D. He, J. Yan, K. Chen, L. Zhang, J. Lu, J. Liu, Y. Luo, Sulfur-Accelerated Ceria Catalyst for Efficient CH_4/CO_2 Reforming: Unraveling the Special Role of Redox Functions and Its Reaction Mechanism, *ACS Catalysis*, 2023, **13**, 12114-12124, doi: 10.1021/acscatal.3c00752.
[44] Y. Liu, Y. Chen, Z. Gao, X. Zhang, L. Zhang, M. Wang, B. Chen, Y. Diao, Y. Li, D. Xiao, X. Wang, D. Ma, C. Shi, Embedding high loading and uniform Ni nanoparticles into silicalite-1 zeolite for dry reforming of methane, *Applied Catalysis B: Environmental*, 2022, **307**, 121202, doi: 10.1016/j.apcatb.2022.121202.
[45] M. Moulana Kareem, M. Hari Babu, G. Vijaya Lakshmi, Anticancer, antibacterial, antioxidant, and photo-catalytic activities of eco-friendly synthesized Ni nanoparticles, *Inorganic Chemistry Communications*, 2023, **148**, 110274, doi: 10.1016/j.inoche.2022.110274.
[46] M. I. Din, M. Tariq, Z. Hussain, R. Khalid, Single step green synthesis of nickel and nickel oxide nanoparticles from hordeum vulgare for photocatalytic degradation of methylene blue dye, *Inorgic Nano-Metal Chemistry*, 2020, **50**, 292–297, doi: 10.1080/24701556.2019.1711401.
[47] S. Hu, W. X. Li, Sabatier principle of metal-support interaction for design of ultrastable metal nanocatalysts, *Science*, 2021, **374**, 6573, 1360–1365, doi: 10.1126/science.abi98.
[48] K. Lorber, J. Zavašnik, J. Sancho-Parramon, M. Bubaš, M. Mazaj, P. Djinović, On the mechanism of visible-light accelerated methane dry reforming reaction over Ni/CeO_{2-x} catalysts, *Applied Catalysis B: Environmental*, 2022, **301**, 120745, doi: 10.1016/j.apcatb.2021.120745.
[49] Z. Di, H. Chen, R. Zhang, H. Wang, J. Jia, Y. Wei, Significant promotion of reducing treatment on of visible-light accelerated methane dry purification at ambient temperature, *Applied Catalysis B: Environmental*, 2022, 304, 120843, doi: 10.1016/j.apcatb.2021.120843.
[50] T. Cao, W. Li, J. Zhu, G. Zhang, H. Liu, K. Wang, G. Kong, Q. Cheng, B. Zhang, X. Zhang, L. Han, Transforming lignin into functionalized B/N co-doped porous carbon for high-performance zinc-ion hybrid capacitors, *Energy Conversion and Management*, 2025, **326**, 119498, doi: 10.1016/j.enconman.2025.119498.
[51] Z. Al-Hamamre, M. Alnaief, J. Yamin, I. Altarawneh, A. Sandouqa, R. Hammouri, A. Nasr, H. Maleki, R. A. Shawabkeh, Synthesis, characterization, and performance evaluation of different sulfonated lignin-based carbon catalysts for upgrading waste vegetable oil to biodiesel, *Energy Conversion and Management*, 2025, **325**, 119381, doi: 10.1016/j.enconman.2024.119381.
[52] D. He, Y. Zhang, T. Li, D. Chen, H. Wang, L. Zhang, J. Liu, X. Cao, J. Lu, Y. Luo, Seidel-Morgenstern, Designing Ultra-Stable and Surface-Exposed Ni Nanoparticles with Dually Confined Microenvironment for High-Temperature Methane Dry Reforming, *Advanced Functional Materials*, 2024, **35**, 2412895, doi: 10.1002/adfm.202412895.
[53] J. Wang, Y. Fu, W. Kong, F. Jin, J. Bai, J. Zhang, Y. Sun,

Design of a carbon-resistant Ni@S-2 reforming catalyst: Controllable Ni nanoparticles sandwiched in a peasecod-like structure, *Applied Catalysis B: Environmental*, 2021, **282**, 119546, doi: 10.1016/j.apcatb.2020.119546.

[54] F. Namvar, M. Salavati-Niasari, F. Meshkani, Effect of the Rare Earth Metals (Tb, Nd, Dy) addition for the modification of nickel catalysts supported on alumina in CO_2 Methanation, *International Journal of Hydrogen Energy*, 2023, **48**, 1877–1891, doi: 10.1016/j.ijhydene.2022.10.096.

[55] G. I. Siakavelas, N. D. Charisiou, A. Al Khoori, S. Al Khoori, V. Sebastian, S. J. Hinder, M. A. Baker, I.V. Yentekakis, K. Polychronopoulou, M.A. Goula, Highly selective and stable Ni/La-M (M=Sm, Pr, and Mg)-CeO_2 catalysts for CO_2 methanation, *J CO_2 Utilization,* 2021, **51**, 101618, doi: 10.1016/j.jcou.2021.101618.

[56] J. Deng, K. Bu, Y. Shen, X. Zhang, J. Zhang, K. Faungnawakij, D. Zhang, Cooperatively enhanced coking resistance via boron nitride coating over Ni-based catalysts for dry reforming of methane, *Applied Catalysis B: Environmental*, 2022, **302**, 120859, doi: 10.1016/j.apcatb.2021.120859.

[57] J. Zhang, B. Ren, G. Fan, L. Yang, F. Li, Exceptional low-temperature activity of a perovskite-type $AlCeO_3$ solid solution-supported Ni-based nanocatalyst towards CO_2 methanation, *Catalysis Science Technology*, 2021, **11**, 3894–3904, doi: 10.1039/D1CY00340B.

[58] B. Hu, Q. Sun, C. Zuo, Y. Pei, S. Yang, H. Zheng, F. Liu, A highly efficient porous rod-like Ce-doped ZnO photocatalyst for the degradation of dye contaminants in water, *Beilstein Journal of Nanotechnology*, 2019, **10**, 1157−1165, doi: 10.3762/bjnano.10.115.

[59] H. Zhang, W. Luo, H. Sun, H. Yang, T. Yang, D. Liu, X. Zhu, L. Zhao, M. Shu, F. Yang, Ce-Doped Nanosheet as Visible Light Photocatalyst for the Photocatalytic Degradation of Tetracycline Hydrochloride, *ACS Applied Nano Material*, 2024, **7**, 11506−11517, doi: 10.1021/acsanm.4c01096.

[60] Y. Zhang, J. Liu, G. Zhang, X. Zhang, Y. Wang, Y. Zhao, G. Li, Ni/MSS@CeO_2 sandwich catalysts for methane dry reforming: the role of reduction on oxygen vacancies, *Journal of Colloid Interface Science*, 2025, **694**, 137712, doi: 10.1016/j.jcis.2025.137712.

[61] W. Liang, G. Xu, Y. Fu, Selective photocatalytic oxidation of furfural to C_4 compounds with metal-TS-1 zeolite, *Applied Catalysis B: Environmental*, 2024, **340**, 123220, doi: 10.1016/j.apcatb.2023.123220.

[62] Y. Sun, G. Li, Y. Gong, Z. Sun, H. Yao, X. Zhou, Ag and TiO_2 nanoparticles comodified defective zeolite TS-1 for improved photocatalytic CO_2 reduction, *Journal of Hazardous Materials*, 2021, **403**, 124019, doi: 10.1016/j.jhazmat.2020.124019.

[63] Z. Yang, L. Li, X. Yang, H. Xiong, R. Zhang, Z. Jiang, Ni-CeO_2/TS-1 catalyze methane dry reforming: Improving catalytic performance and stability by modulating the amount and strength of Ni-O-X species, *Chemical Engeering Journal*, 2024, **497**, 154594, doi: 10.1016/j.cej.2024.154594.

[64] T. Tan, Y. Chen, Y. Wang, Z. Li, Z. Zhang, J. Xie, Y. Chen, Insight into the effects of the CO_2/H_2O activation and Ce redox cycle over ni/CeO_2/hydrotalcite catalyst surface on biogas Bi-reforming for methanol friendly syngas, *Energy*, 2024, **313**, 133954, doi: 10.1016/j.energy.2024.133954.

[65] Z. Li, W. Bai, D. Liu, B. Han, Y. Liang, J. Qi, Preloaded oxygen vacancy conditioning Ni/TiO_2 to enhance photocatalytic CO_2 reduction, *Separation and Purification Technology*, 2024, **330**, 125250, doi: 10.1016/j.seppur.2023.125250.

[66] F. Cai, G. Xiao, Promoting effect of Ce on a Cu-Co-Al catalyst for the hydrogenolysis of glycerol to 1, 2-propanediol, *Catalysis Science Technology*, 2016, **6**, 5656−5667, doi: 10.1039/C6CY00116E.

[67] W. H. Wang, B. Jiang, Z. Wang, Y. Chen, Y. Li, T. T. Luo, F. Cheng, B. L. Su, Alloying effect enhanced bimetallic Ni-Fe/TiO_2 catalysts for selective hydrogenation of 1,3- butadiene in the presence of an excess of propylene, *Molecular Catalysis*, 2023, **550**, 113602, doi: 10.1016/j.mcat.2023.113602.

[68] R. Khatun, R. S. Pal, M. A. Shoeb, D. Khurana, S. Singhl, N. Siddiqui, M. K. Poddar, T. S. Khan, R. Bal, Generation of active oxygen species by CO_2 dissociation over defect-rich Ni-Pt/CeO_2 catalyst for boosting methane activation in lowtemperature dry reforming: Experimental and theoretical study, *Applied Catalysis B: Environmental*, 2024, **340**, 123243, doi: 10.1016/j.apcatb.2023.123243.

[69] P. D. Hong, K. S. Zhang, J. Y. He, Y. L. Li, Z. J. Wu, C. Xie, J. H. Liu, L. T. Kong, Selenization governs the intrinsic activity of copper-cobalt complexes for enhanced non-radical Fenton-like oxidation toward organic contaminants. *Journal of Hazardous Materials*, 2022. **435**, 128958. doi: 10.1016/j.jhazmat.2022.128958.

[70] H. Sun, A. Xie, X. Zhang, H. Zhang, H. Yang, S. Xie, Z. Jiang, L. Zhao, Q. Niu, W. Zhou, F. Yang, Praseodymium-regulated microregion electron structures of Bi2WO6 nanosheets to construct non-radical platforms for the photocatalytic decontamination of water by hydrogen peroxide activation, *Environmental Research*, 2025, **280**, 121919. dol: 10.1016/j.envres.2025.121919.

[71] J. Xu, P. Xia, F. Guo, J. Xie, Y. Xia, H. Tian, Enhancement of the catalytic performance and coke resistance of alcohol-promoted Ni/MCM-41 catalysts for CH_4/CO_2 reforming, *International Journal of Hydrogen Energy*, 2020, **45**, 30484–30495, doi: 10.1016/j.ijhydene.2020.08.050.

[72] J. S. Bitters, T. He, E. Nestler, S. D. Senanayake, J. G. Chen, C. Zhang, Utilizing bimetallic catalysts to mitigate coke formation in dry reforming of methane, *Journal of Energy Chemistry*, 2022; **68**, 124-142, doi: 10.1016/j.jechem.2021.11.041.

[73] Q. Zhang, Z. Jiang, Y. Zhang, X. Xu, Y. Yang, Y. Qin, L. Song, Y. Mei, Y. Zu, Deciphering transient carbon footprint for methane dry reforming over Ni@S-1 nanosheet zeolite catalyst, *Applied Catalysis B: Environmental and Energy*, 2025, **362**, 124722, doi: 10.1016/j.apcatb.2024.124722.

[74] C. Vogt, J. Kranenborg, M. Monai, B. M. Weckhuysen, Structure Sensitivity in Steam and Dry Methane Reforming over Nickel: Activity and Carbon Formation, *ACS Catalysis*, 2020, **10**,

1428-1438, doi: 10.1021/acscatal.9b04193.
[75] J. Tian, H. Li, X. Zeng, Z. Wang, J. Huang, C. Zhao, Facile immobilization of Ni nanoparticles into mesoporous MCM-41 channels for efficient methane dry reforming, *Chinese Journal of Catalysis*, 2019, **40**, 1395–1404, doi: 10.1016/S1872-2067(19)63403-0.
[76] M. A. Vasiliades, C.M. Damaskinos, P. Djinović, A. Pintar, A.M. Efstathiou, Dry reforming of CH4 over NiCo/$Ce_{0.75}Zr_{0.25}O_{2-\delta}$: The effect of Co on the site activity and carbon pathways studied by transient techniques, *Catalysis Communications*, 2021, **149**, 106237, doi: 10.1016/j.catcom.2020.106237.
[77] H. Chen, S. Chansai, S. Xu, S. Xu, Y. Mu, C. Hardacre, X. Fan, Dry reforming of methane on bimetallic Pt-Ni@CeO_2 catalyst: A in situ DRIFTS-MS mechanistic study, *Catalysis Science Technology*, 2021, **11**, 5260–5272, doi: 10.1039/D1CY00382H.
[78] V. K. Velisoju, Q. J. S. Virpurwala, Y. Attada, X. Bai, B. Davaasuren, M. Ben Hassine, X. Yao, G. Lezcano, S.R. Kulkarni, P. Castano, Overcoming the kinetic and deactivation limitations of Ni catalyst by alloying it with Zn for the dry reforming of methane, *J CO_2 Utilization,* 2023, **75**, 102573, doi: 10.1016/j.jcou.2023.102573.